Extended Catalog of Winged or X-shaped Radio Sources from the FIRST Survey

The Astrophysical Journal Supplement Series, 245:17 (25pp), 2019 November https://doi.org/10.3847/1538-4365/ab4811

Extended Catalog of Winged or X-shaped Radio Sources from the FIRST Survey

Xiaolong Yang[1], Ravi Joshi[1], Gopal-Krishna[2,3], Tao An[4], Luis C. Ho[1,5], Paul J. Wiita[6], Xiang Liu[7], Jun Yang[4,8], Ran Wang[1,5], Xue-Bing Wu[1,5], and Xiaofeng Yang[7]

[1] Kavli Institute for Astronomy and Astrophysics, Peking University, Beijing 100871, People's Republic of China; yxl.astro@gmail.com
[2] Aryabhatta Research Institute of Observational Sciences (ARIES), Manora Peak, Nainital—263002, India
[3] UM-DAE Centre for Excellence in Basic Sciences, University of Mumbai, Mumbai—400098, India
[4] Shanghai Astronomical Observatory, Key Laboratory of Radio Astronomy, Chinese Academy of Sciences, 200030 Shanghai, People's Republic of China
[5] Department of Astronomy, School of Physics, Peking University, Beijing 100871, People's Republic of China
[6] Department of Physics, The College of New Jersey, P.O. Box 7718, Ewing, NJ 08628-0718, USA
[7] Xinjiang Astronomical Observatory, Key Laboratory of Radio Astronomy, Chinese Academy of Sciences, 150 Science 1-Street, 830011 Urumqi, People's Republic of China
[8] Department of Earth and Space Sciences, Chalmers University of Technology, Onsala Space Observatory, SE-43992 Onsala, Sweden
Received 2019 May 14; revised 2019 September 23; accepted 2019 September 24; published 2019 November 15

Abstract

We present a catalog of 290 "winged" or X-shaped radio galaxies (XRGs) extracted from the latest (2014 December 17) data release of the "Very Large Array Faint Images of the Radio Sky at Twenty centimeter." We have combined these radio images with their counterparts in the TIFR GMRT sky survey at 150 MHz, in an attempt to identify any low surface brightness radio emission present in these sources. This has enabled us to assemble a sample of 106 "strong" XRG candidates and 184 "probable" XRG candidates whose XRG designation needs to be verified by further observations. The present sample of 290 XRG candidates is almost twice as large as the number of XRGs currently known. Twenty-five of our 290 XRG candidates (9 "strong" and 16 "probable") are identified as quasars. Double-peaked narrow emission lines are seen in the optical spectra of three of the XRG candidates (two "strong" and one "probable"). Nearly 90% of the sample is located in the FR II domain of the Owen–Ledlow diagram. A few of the strong XRG candidates have a rather flat radio spectrum (spectral index α flatter than -0.3) between 150 MHz and 1.4 GHz, or between 1.4 and 5 GHz. Since this is not expected for lobe-dominated extragalactic radio sources (like nearly all known XRGs), these sources are particularly suited for follow-up radio imaging and near-simultaneous measurement of the radio spectrum.

Unified Astronomy Thesaurus concepts: Active galactic nuclei (16); Jets (870); Quasars (1319); Radio continuum emission (1340); Catalogs (205); Surveys (1671)

1. Introduction

Active galactic nuclei (AGNs) are long believed to be located at the centers of massive galaxies (e.g., Kormendy & Ho 2013). A plausible scenario to account for the enormous energy release from the AGN involves accretion of matter onto a supermassive black holes (SMBH), which, under suitable conditions, can also result in the launch of a pair of relativistic jets of nonthermal radio emission, which can extend up to megaparsec dimensions (e.g., Heckman & Best 2014; Dabhade et al. 2017). Such galaxies, referred to as "radio galaxies" (RGs), often show a compact radio core flanked by a pair of "radio lobes." Nearly always, powerful RGs are associated with elliptical galaxies (Véron-Cetty & Véron 2001). Remarkably, a small minority of RGs are known to exhibit *two pairs* of fairly well collimated radio lobes, broadly forming an X-shaped morphology. These "winged" or "X-shaped" radio galaxies (XRGs; e.g., Leahy & Parma 1992) form the topic of this work.

XRGs constitute about 5%–10% of radio galaxies in the 3CRR catalog (Leahy & Williams 1984; Leahy & Parma 1992). Based on an edge-darkened or edge-brightened radio morphology of the brighter (i.e., primary) radio lobe pair, they are classified as Fanaroff-Riley type I (FR I) or type II (FR II) XRGs, respectively (Fanaroff & Riley 1974). Recall that whereas a pair of radio lobes, each having a "hot spot" near its outer edge, is seen in FR II sources, FR I sources often exhibit a jet pair emanating from a prominent radio core, each jet forming an edge-darkened radio lobe. The primary lobe pair in a majority of XRGs in the Leahy & Parma (1992) sample belong to the FR II type, whereas the secondary lobes ("wings") in all known XRGs are of the FR I type. Also, interestingly, radio luminosities of XRGs are mostly near the FR I and FR II division ($P_{178\,\mathrm{MHz}} \approx 2 \times 10^{25}$ W Hz^{-1} sr^{-1}; e.g., Cheung et al. 2009; Landt et al. 2010). Their intermediate radio luminosities may hint that XRGs represent a transitional morphology between the FR I and FR II types (Landt et al.2010).

The origin of XRGs is contentious, and several models have been proposed to explain this phenomenon, as reviewed in Gopal-Krishna et al. (2012). The three most discussed scenarios for their formation are (1) diversion of the back-flowing synchrotron plasma of the radio lobes, upon impacting an asymmetric circumgalactic gaseous halo of the parent early-type galaxy; (2) precession of the (large-scale) twin jets; and (3) spin-flip of the central SMBH.

In the backflow model, the radio wings form owing to diversion of the backflowing lobe plasma, whose subsequent outward expansion is aided by the buoyancy forces exerted by a steep pressure gradient in the circumgalactic medium (CGM) of the parent galaxy (Leahy & Williams 1984; Worrall et al. 1995; Kraft et al. 2005; Miller & Brandt 2009), the diversion occurring preferentially into preexisting cavities/channels in the CGM (Leahy & Williams 1984; Machalski et al. 2016). However, Leahy & Parma (1992) have cautioned that buoyancy-driven backflow cannot propagate faster than the external sound speed, and hence the wings propelled by the buoyancy forces are not expected to be longer than the main radio lobes (which are known to advance supersonically). Since this is not

always the case, a possible resolution may lie in the possibility that overpressured cocoons can drive supersonic outflows of the backflowing lobe plasma, forming gigantic radio wings (Capetti et al. 2002; Hodges-Kluck & Reynolds 2011; Rossi et al. 2017). In order to realize the needed large overpressure relative to the ambient medium, the jet's head would be required to first propagate out to sufficiently large distance from the nucleus.

Observational support to the backflow deflection model comes from optical studies of the host galaxies of XRGs (Capetti et al. 2002; Saripalli & Subrahmanyan 2009; Gillone et al. 2016). These studies have demonstrated that the radio axis defined by the two primary lobes displays a preference to align with the optical *major* axis of the host elliptical galaxy. The two wings (secondary lobes) show a strong tendency to align with the *minor* axis of the optical host, which is consistent with the expectation that the putative buoyancy-driven expansion of the wings should occur along the maximum pressure gradient. In tune with this basic picture, XRGs are found to be associated predominantly with early-type galaxies whose ellipticity is abnormally high (Gillone et al. 2016, and references therein). The strong statistical correlation observed between the host galaxy properties and the X-shaped radio morphology provides support to the overpressured lobe scenario, and this is corroborated by the available X-ray images of a few XRGs, which trace the (asymmetric) shape of their CGM (Hodges-Kluck et al. 2010a).

Taking a clue from the observed S-shaped radio morphologies of the nearby radio galaxies Centaurus A and 3C 272.1, Ekers et al. (1978) proposed that geodetic precession of the jet pair, conceivably due to a torque exerted by an external massive body, can explain the huge Z-symmetric radio trails extending from the extremities of the two lobes of the giant radio galaxy NGC 326. The jet precession may also be caused by a tilted and warped accretion disk (see Caproni et al. 2006, and references therein), or by a close passage of a neighboring galaxy (Blandford & Icke 1978; Dennett-Thorpe et al. 2002). Indeed, Battistini et al. (1980) reported that NGC 326 is associated with a dumbbell galaxy, i.e., two nearly equally bright ellipticals within a common envelope, of which one is currently hosting jet activity and interacting gravitationally with its elliptical neighbor (Murgia et al. 2001). A study of ∼100 radio sources associated with dumbbell galaxies has in fact revealed markedly distorted radio structures in roughly a dozen of them (Wirth et al. 1982). In this picture, the interacting neighbor may be in either a highly eccentric (or unbound) orbit or a circular orbit. In the first case, impulsive gravitational interaction can lead to an inversion-symmetric distortion of the jet pair, resulting in an X-shaped or Z-shaped morphology. In the second case, the continued tidal interaction can cause periodic inversion-symmetric wiggles in the radio jet pair, giving rise to a helical radio morphology. A warped and tilted accretion disk can also be expected to form in SMBH binaries, leading to an X-shaped radio morphology (Begelman et al. 1980). One motivating factor behind this scenario is the discovery of double-peaked emission lines in the optical spectra of a few XRGs (Zhang et al. 2007). By modeling the radio morphological distortions observed in three XRGs (3C 52, 3C 223.1, and 4C 12.03), Gong et al. (2011) have estimated precession periods of the order of a million years; such a timescale would be consistent with the estimated dynamic ages of active radio lobes and the wings in XRGs (Mezcua et al. 2012).

In the "spin-flip" scenario, the wings of an XRG are regarded as the fossil synchrotron plasma of the earlier (pre spin-flip) lobe pair, while the observed misalignment of the currently "active" lobes from the axis defined by the wing pair is attributed to the jet's reorientation, following a sudden tilt of the spin axis of the AGN's SMBH resulting from coalescence of the two SMBHs belonging to the pair of merging galaxies (Rottmann 2001; Zier & Biermann 2001; Merritt & Ekers 2002). However, it has also been argued that the wings could even form prior to the SMBH merger (Biermann et al. 2002; Gopal-Krishna et al. 2003; Zier 2005). In a systematic study, Mezcua et al. (2011) have found that the host ellipticals of nearly half of the XRGs exhibit signatures of a starburst occurring around 10^9–$10^{9.5}$ yr (1–3 Gyr) ago. Hydrodynamical simulations of galaxy mergers suggest a time interval of about 2 Gyr between a merger-induced starburst and the onset of AGN activity (Lotz et al. 2008), in accord with the idea of a physical link between galaxy merger and XRG formation. There exist other observational evidences implicating galaxy mergers in the XRG formation. These include the following: (1) elliptical galaxies hosting XRGs have SMBHs of larger than average mass found using a control sample of elliptical galaxies (Mezcua et al. 2011); and (2) detection of X-ray cavities and a likely stellar shell in the XRG system 4C +00.58 (Hodges-Kluck et al. 2010b), as well as the detection of shells around the host galaxy of the XRG 3C 403 (Ramos Almeida et al. 2011). Also, a recent dynamical analysis of the hybrid radio structural distortion observed in the radio galaxy 3C 293 lends support to the rapid jet realignment scenario for XRGs (Machalski et al. 2016). On the other hand, the merger-induced rapid reorientation model encounters difficulty in explaining the strong tendency for the wings of XRGs to align with the optical minor axis of the host galaxy (Gillone et al. 2016, and references therein).

It is important to bear in mind that none of the above models are capable of consistently explaining the entire gamut of observed properties of XRGs, as emphasized in a review of XRG models, which also dwells on a few alternative explanations (Gopal-Krishna et al. 2012). One of these alternatives invokes a collision between the radio jet pair and the (partial) shells around the host elliptical, which are believed to form in the process of galaxy merger (see Gopal-Krishna & Chitre 1983; Gopal-Krishna & Saripalli 1984; Zier 2005). A possible substitute for the shells is the interstellar medium of the massive host elliptical, which is set in rotation by a captured galaxy as it spirals inward in the course of its merger with the massive elliptical (Gopal-Krishna et al. 2003). A distinct merit of this model lies in its ability to provide a natural explanation for the Z-shaped morphology traced by the radio wings, a pattern highlighted in that study, where it was noted to be a fairly common feature of the XRGs with well-resolved radio maps. Yet another explanation proposed for the XRGs simply posits that the nucleus possesses not one but two SMBHs, each of which ejects a jet pair grossly misaligned from the other (Lal et al. 2008; see also Lal et al. 2019). This would have been the most direct explanation for XRGs, except for the difficulty it faces in explaining the observed Z-symmetry of the wings (see above), the observed preferential alignment of the wing pair with the optical minor axis of the host galaxy, and the fact that hot spots are never found in *both* pairs of radio lobes in XRGs (see, e.g., Gopal-Krishna et al. 2003). Furthermore, VLBI observations of XRGs have so far provided no compelling evidence for dual active nuclei inside the radio core (Burke-Spolaor 2011).

The striking diversity of the different models proposed for the origin of XRGs makes them an extraordinarily interesting subclass of radio galaxies. In addition, they carry special astrophysical interest by being potential sources of gravitational waves, if indeed the "spin-flip" model is the correct description for at least a substantial fraction of XRGs (Heckman et al. 1986; Rottmann 2001; Biermann et al. 2002; Merritt & Ekers 2002; Milosavljević & Merritt 2003; Roberts et al. 2015a), Thus, an improved estimation of the fraction of RGs that turn into XRGs via the spin-flip route would enable realistic predictions for the low-frequency gravitational wave background that is thought to pervade the universe (e.g., Roberts et al. 2015b, and references therein).

The studies mentioned above are constrained owing to the rather small sizes of the available XRG samples. The first major step toward rectifying this problem was taken by Leahy & Parma (1992). Later, Cheung (2007, hereinafter C07) identified 100 XRG candidates from a systematic search in the FIRST survey catalog (Becker et al. 1995). Their search was limited to sources with radio major-axis size larger than 15″, expectedly resulting in a significant underrepresentation of the XRG population in their list. Furthermore, the available optical and radio details are highly incomplete even for that sample. For instance, out of the 100 XRGs in the C07 sample, only ∼50% have been observed spectroscopically (Cheung et al. 2009, hereafter C09; Mezcua et al. 2012), and only 53 out of the 100 XRGs have been taken up for investigating the host galaxy properties (Gillone et al. 2016). Similarly, analyses of the SMBH mass and starburst history (Mezcua et al. 2011) have been reported for just 29 out of the 100 XRGs, and merely 12 of them are covered in the follow-up study by Mezcua et al. (2012). Therefore, in order to enlarge the scope of the studies of XRGs, it is desirable to extend the XRG search campaign initiated by Cheung (2007). We have undertaken such a search program by lowering the radio source size threshold for XRG candidates from 15″ employed in that study to 10″. Based on this revised size threshold, we present here a new catalog of candidate X-shaped radio sources, drawn from the latest data release of the FIRST survey at 1.4 GHz (Becker et al. 1995). In Section 2, we briefly comment on the existing XRG catalogs. Details of our selection procedure and the main results of our campaign are presented in Section 3. The host galaxy identification and radio properties are described in Sections 4 and 5, followed by a brief discussion (Section 6) and a summary of the present results (Section 7). Throughout this paper, we assume a ΛCDM cosmology with parameters $H_0 = 70$ km s^{-1} Mpc^{-1}, $\Omega_\Lambda = 0.7$, and $\Omega_m = 0.3$.

2. Existing Lists and Definition of the "Winged" or "X-shaped" Radio Sources

As a class, X-shaped extragalactic radio sources were first discussed by Leahy & Parma (1992), based on their list of 11 XRGs. Of these, the primary lobe pair showing a clear FR II radio morphology with well-defined hot spots is seen in seven sources. Cheung (2007) collected another eight XRGs through a literature search, raising the sample to 19 XRGs. The first systematic search for the XRGs was undertaken by Cheung (2007, C07), based on the VLA FIRST survey (Becker et al. 1995). He compiled an initial list of 100 XRG candidates showing a "winged" or X-shaped radio morphology, by visually inspecting 1648 sources in which at least a hint of inversion-symmetric radio lobe structure was present and the primary lobes extend more than 15″. Recently, Roberts et al. (2018) have reported JVLA multi-array (mainly A-array) radio continuum imaging in the L and/or C band of XRG candidates from C07. Based on these observations, Saripalli & Roberts (2018) have subsequently identified 12 sources as S- or Z-shaped radio galaxies. Remarkably, more than 75% of the C07 sample has turned out to be bona fide XRGs and hence very useful for probing the question of the origin of XRGs (see Cheung et al. 2009; Mezcua et al. 2011, 2012; Gillone et al. 2016).

A more recent XRG search is reported in Proctor (2011), who applied an automated morphological classification scheme to the FIRST radio sources. Adopting a separation cut of 0.′96 arcmin, they classified the radio sources into singles, doubles, triples, and groups of higher membership count. They also visually inspected 7106 higher-count group members, thus finding 156 candidates for X-shaped radio morphology. Out of these, 21 sources had already been reported in C07, and one object, 3C 315, is a well-known XRG (see below), leaving 134 new XRG candidates (this is ∼2% of the sources classified by them as higher-count groups). Two of us (R.J. and X.L.Y.) have visually inspected the 156 XRG candidates reported in Proctor (2011), in search of an unambiguous X-shaped morphology with well-defined wings (see Section 6.1 for details of our selection procedure), and assessed 43 of them to be strong XRG candidates and the remaining systems as the probable candidates. Out of these 43 strong candidates, 18 sources are common to C07, and FCG J151340.0 +260730 (3C 315) is the archetypal XRG, known for over four decades (Mackay 1969; Hogbom & Carlsson 1974). Thirteen of the remaining 24 sources were also picked in the present search for strong XRG candidates in the 2014 December 17 release of the FIRST catalog, and these are marked with an asterisk in Column (1) of Table 2, while 11 were not because they did not fulfill our criterion that the radio major and minor axes should be greater than 10″ and 5″, respectively—see Section 3.1.

It is worth emphasizing that even though the visual inspection approach for picking XRG candidates is beset with subjectivity, it does yield promising XRG candidates, as validated by the high (>75%) confirmation rate of the XRG candidates reported in C07 (e.g., Roberts et al. 2018; Saripalli & Roberts 2018). Recalling the standard definition, the XRGs are a subset of radio sources that exhibit an additional (fainter) pair of radio lobes displaying an inversion-symmetric configuration. These "secondary" radio lobes, often called "wings," are aligned at a fairly large angle from the main radio axis defined by the primary lobe pair. Conventionally, the readily accepted examples of XRGs are those in which the wings extend to at least 80% of the size of the primary lobes. However, since the wings always lack a brightness peak (hot spot) near the extremity, their measured radio extents (and hence the robustness of their XRG classification) would depend sensitively on the depth and spatial resolution of the radio map. For instance, although only one wing of the well-known XRG 3C 63 is apparent in the 1.4 GHz VLA B-array map (Baum et al. 1988), both wings clearly stand out in its subsequent VLA A-array image at 1.4 GHz (Harvanek & Hardcastle 1998). Similarly, the large, prominent wings present in the radio maps of the well-known XRGs 3C 192 and 3C 379.1 (Myers & Spangler 1985; Baum et al. 1988; Dennett-Thorpe et al. 1999) only appear as short extensions in their earlier shallower radio maps (Myers & Spangler 1985; Leahy et al. 1997). Furthermore, it now appears quite plausible that XRGs are morphological cousins of Z-shaped radio galaxies, in which the oppositely directed wings launch out from the main radio axis at locations that are relatively close to the host galaxy (e.g., Gopal-Krishna et al. 2003). Thus, in isolation, the two wings can often be described as a Z-shaped double radio source (Gopal-Krishna

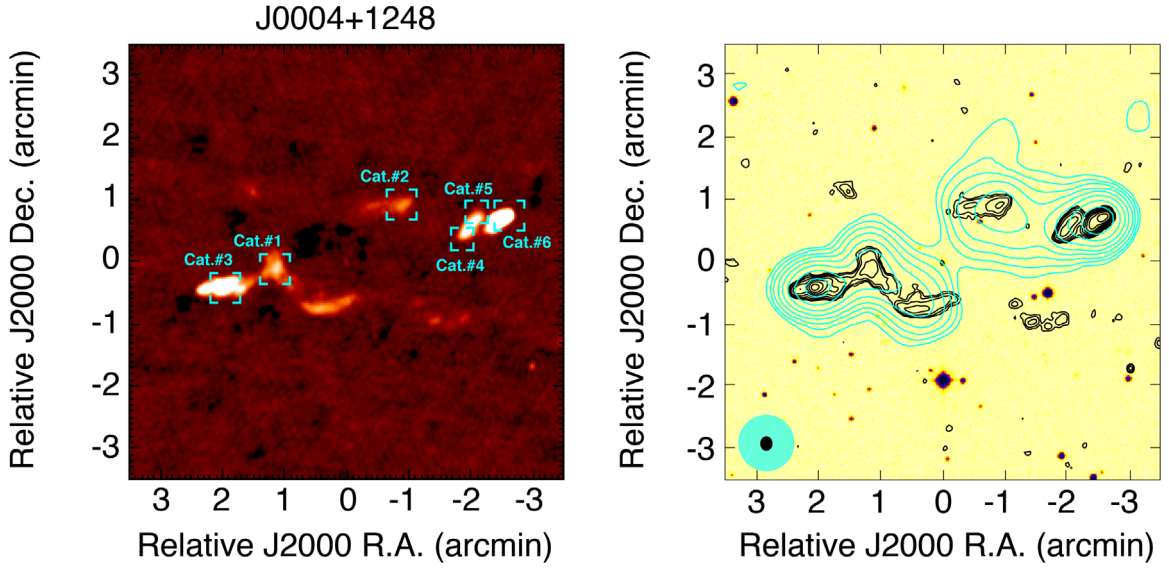

Figure 1. Radio structure of a representative giant X-shaped radio source hosted by a galaxy at the field center with R.A. = 00:04:50.27 (J2000), decl. = +12:48:39.5 (J2000). Left panel: the radiograph with all the FIRST catalog entries that satisfied our selection criteria marked (see Table 1). Right panel: black contours are from the VLA FIRST survey at 1.4 GHz; cyan contours are from the GMRT TGSS_ADR1 survey at 150 MHz. The TGSS_ADR1 and FIRST contour levels are set at 0.6 × and 10 × (1, 2, 4, 8, 16, ...) mJy beam^{-1}, respectively. In the lower left corner, the synthesized beams (cyan for the TGSS_ADR1 and black for the FIRST contours) are indicated by ellipses.

et al. 2003). Guided by all these considerations and in order to minimize missing out genuine XRGs, we have resorted to a somewhat less conservative approach in assembling the present catalog of XRG candidates, by also including the sources showing short wings (or even a one-sided wing), or just a hint of X-shaped radio structure. This was followed up by classifying them as "strong" and "probable" XRG candidates (Section 6.1). Clearly, the latter would inevitably need higher-quality radio images for validation as genuine XRGs.

3. Searching for X-shaped Radio Sources in the Latest Release of the FIRST Survey

We have assembled the present catalog of 290 XRG candidates by searching in the latest VLA FIRST survey data release version 14Dec17.[9] This version covers 10,575 deg^2 of the sky (8444 deg^2 in the northern hemisphere and 2131 deg^2 in the southern hemisphere) and contains 946,432 radio sources, including those reported in the earlier data releases from 1993 through 2011. The survey achieved a typical rms noise of 0.15 mJy and a resolution of ∼5″ at 1.4 GHz (Becker et al. 1995). The main product of the FIRST survey is a radio intensity map of the sky, including a catalog of discrete radio sources from the co-added images (White et al. 1997). The catalog also lists for each entry the peak and integrated flux densities and angular size at 1.4 GHz, derived from fitting two-dimensional Gaussians. Note that in the FIRST catalog an extended radio source can often have multiple entries (Proctor 2003, 2006; see also Figure 1). As estimated by Proctor (2011), ∼30% of the entries are actually individual multicomponent radio sources, which offers a huge database for morphological studies.

3.1. Basic Sample Selection

Given the enormous size of the FIRST catalog and the abundance of multicomponent systems in it (see, e.g., Figure 1 and Table 1), examining the map of each source is not a practical option. Therefore, we first extracted a subset of XRG candidates by demanding (1) a peak flux density sufficiently high to realize an acceptable dynamic range and (2) a radio extent sufficiently large to reveal the basic morphological features. Below, we describe our sample selection procedure in some detail.

The characteristic feature of XRGs is two (misaligned) pairs of radio lobes/jets, such that there is a large angular offset between the axes defined by the brighter (primary) lobe pair and by the two secondary lobes (i.e., "wings"), whose surface brightness is usually much lower. Only the primary lobes are known to exhibit an edge-brightened morphology, i.e., a hot spot typically situated near the lobe's extremity. Considering the typical rms noise of the FIRST maps (0.15 mJy beam^{-1}), a 3σ detection threshold would correspond to a minimum peak flux density of 0.45 mJy beam^{-1}. Here we make a reasonable assumption that the peak brightness of the hot spots in the primary lobes is about 10 times the (average) surface brightness of the wings. Accordingly, as the first selection filter, we set a lower limit of 5 mJy beam^{-1} for the peak flux density at 1.4 GHz. This would normally permit a minimum dynamic range of ∼33:1, and one may thus reasonably expect to detect

Table 1
FIRST Catalog Entry for Each Component in the Field J000450.27+124839.5 (See Figure 1)

Component	Peak Flux (mJy beam^{-1})	Major Axis[a] (arcsec)	Minor Axis[a] (arcsec)
Cat.#1	7.80	22.88	15.44
Cat.#2	5.72	14.47	7.64
Cat.#3	20.29	23.41	10.98
Cat.#4	12.56	12.03	7.19
Cat.#5	12.60	14.25	7.59
Cat.#6	56.57	11.28	6.79

Note.
[a] The deconvolved synthesized beam major and minor axes.

[9] Data released on 2014 December 17.

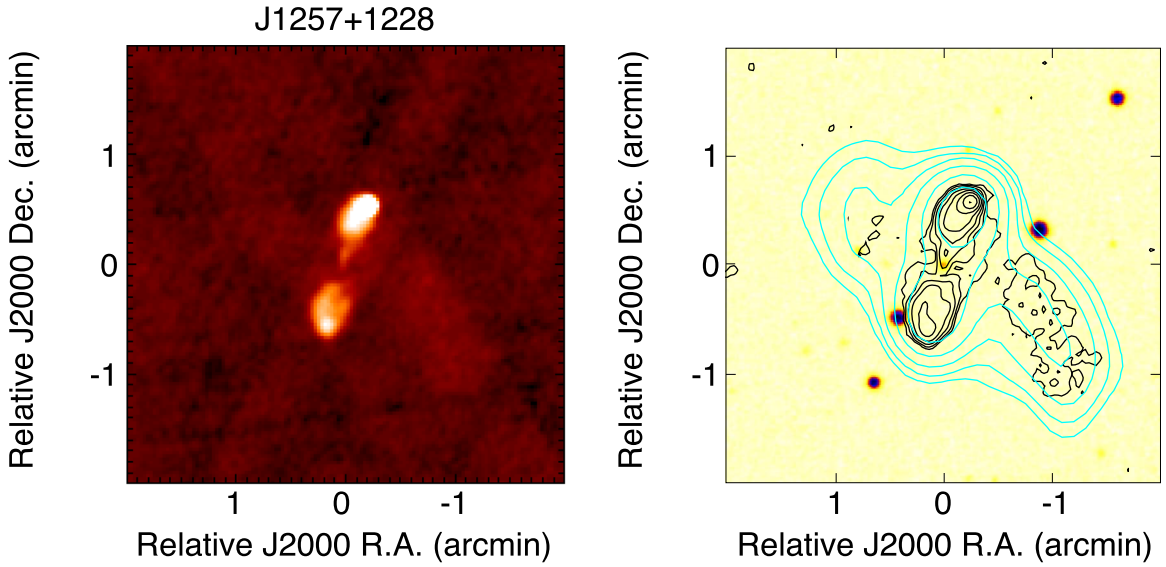

Figure 2. Example of a "strong" XRG candidate in the present catalog: J1257+1228. The left panel shows the FIRST gray-scale image, and the right panel shows the FIRST (black) and TGSS_ADR1 contours (cyan) overlaid on the DSS red filter image. The contours are plotted at (1, 2, 4, 8, 16, 32, ...) × 3σ. The rms (1σ) noise value is 0.14 mJy beam^{-1} for the FIRST contours and 3.5 mJy beam^{-1} for the TGSS_ADR1 contours. This example underscores the importance of combining the 1.4 GHz maps with their 150 MHz counterparts.

any associated wings (see Section 4). Next, in order to minimize missing any wings, we need to ensure that a given source is fairly well resolved with the ∼4.″3 synthesized beam (VLA B array) of the FIRST survey. Hence, our second selection filter is that the radio major ($\theta_{\rm maj}$) and minor ($\theta_{\rm min}$) axes of the fitted Gaussian should be larger than 10″ and 5″, respectively. In this way, the present compilation is an extension of the XRG search reported in C07 (see their Section 3.1). Application of the above two selection filters left us with a basic list of 5128 sources. Of these, 2350 sources have $10'' < \theta_{\rm maj} \leqslant 13''$, 935 sources have $13'' < \theta_{\rm maj} \leqslant 15''$, and the remaining 1843 sources have $\theta_{\rm maj} > 15''$.

3.2. Visual Inspection of the Radio Maps of the Short-listed Sources

In the next step, we queried the radio field for each of the 5128 short-listed sources, from the online archive of the FIRST survey[10] (Becker et al. 1995), with an image size of 6 × 6 arcmin^2. Given the usually complex (multicomponent) radio structures of known XRGs, we decided to also make use of their 150 MHz radio continuum images reported in the first alternative data release of TIFR GMRT Sky Survey[11] (TGSS_ADR1 Intema et al. 2017). Its combination of angular resolution (∼25″) and a low frequency (150 MHz) is better suited for picking up diffuse emission. The source J1257+1228 is a good example here (see Figure 2). It is impossible to tell whether it is an X-shaped winged source based on visual inspection of the FIRST gray-scale image alone, whereas according to the FIRST-based contour map, J1257+1228 is "half X-shaped." Only the TGSS contour map confirms that it is in fact an X-shaped source. Radio contour maps and pseudo-color images were then generated to facilitate the visual inspection (see Appendix Figure 9 for the "strong" XRG candidates). For each field, we measured the rms noise and used it for setting the base level for the contour plotting. We initially used the 3σ level and slightly fine-tuned it in individual cases, so as to minimize the confusion arising from side lobes in the map. For the color images, we have carefully set the brightness to emphasize any wing-like features.

The above procedure was then followed up with two of the coauthors independently inspecting the radio structure of each short-listed source, and their mutual concurrence was treated as the trigger for admitting a given source as a preliminary XRG candidate. In the final round, radio images of all such sources were individually inspected by three of the coauthors, which led to the final list of 290 XRG candidates. Depending on the level of consensus among the three coauthors, these XRG candidates were placed in "strong" (106) or "probable" (184) categories (Tables 2 and 3). The classification is further discussed in Section 6.1. It may be noted that only 25 of these XRG candidates appear in the list of Proctor (2011). Note also that since the present XRG sample is meant to be an extension of the C07 XRG sample, we have decided to retain these 25 XRG candidates, of which 13 systems belong to our list of strong XRG candidates. Those sources are marked with an asterisk in the first column in Tables 2 and 3.

4. Identification of the Host Galaxy and Its Properties

In this key step, we first defined for each source a likely position of the active core, near the symmetry center of its radio structure. The radio contours were then overlaid on the Sloan Digital Sky Survey (SDSS) SDSS *i*-band and/or Digital Sky Survey (DSS) red filter image of the source. For most (∼80%) of our XRG candidates, an optical counterpart could thus be found close to the expected location. For the remaining sources, we have simply used the estimated radio symmetry center as the coordinates of the (undetected) optical counterpart. These coordinates for our 106 "strong" and 184 "probable" XRG candidates are listed in Columns (2) and (3) of Tables 2 and 3, respectively. In Figure 9 (see Appendix) we have displayed the FIRST 1.4 GHz images of our 106 "strong" XRG candidates; the corresponding TGSS_ADR1 150 MHz image is shown in the right panel of each subplot, except for

[10] http://sundog.stsci.edu/index.html
[11] https://vo.astron.nl/tgssadr/q_fits/imgs/form

Table 2
"Strong" X-shaped Radio Source Candidates

Short Name	R.A. (J2000)	Decl. (J2000)	z	Qual.	r	M_R	$S_{i,0.15}$ (Jy)	$S_{i,1.4}$ (Jy)	$S_{i,5}$ (Jy)	Ref.$_{5\ \mathrm{GHz}}$	$\alpha_{0.15}^{1.4}$	$\alpha_{1.4}^{5}$
(1)	(2)	(3)	(4)	(5)	(6)	(7)	(8)	(9)	(10)	(11)	(12)	(13)
J0004+1248	00 04 50.27	+12 48 39.5	0.143	SPEC	17.44	−21.37	…	0.107	0.407	NRAO	…	1.07
J0028−0026[a]	00 28 28.94	−00 26 24.6	0.287	PHOT	18.96	−21.52	…	…	0.390	NRAO	…	…
J0030+1121	00 30 23.86	+11 21 12.5	0.449	SPEC	20.16	−22.06	0.515	0.114	0.136	NRAO	−0.67	0.14
J0121+0051	01 21 01.23	+00 51 00.3	0.238	SPEC	17.80	−22.16	1.124	0.267	0.105	NRAO	−0.64	−0.75
J0216+0244	02 16 35.79	+02 44 00.9	0.184	PHOT	17.58	−21.70	2.650	0.300	0.248	PMN	−0.97	−0.15
J0319−0202[a]	03 19 37.58	−02 02 48.7	…	...	…	…	0.849	0.212	0.080	NRAO	−0.62	−0.78
J0710+3546	07 10 31.14	+35 46 49.8	…	…	…	…	…	0.073	0.030	NRAO	…	−0.71
J0715+4910	07 15 10.12	+49 10 53.2	…	…	…	…	0.513	0.084	0.044	NRAO	−0.81	−0.52
J0720+4037	07 20 14.66	+40 37 48.6	0.387	PHOT	19.87	−21.65	0.628	0.096	0.034	NRAO	−0.84	−0.83
J0727+3956	07 27 37.48	+39 56 55.8	0.312	SPEC	18.25	−22.57	0.217	0.050	…	…	−0.65	…
J0752+3252[a]	07 52 49.10	+32 52 54.2	0.299	PHOT	18.74	−21.94	2.262	0.370	0.120	NRAO	−0.81	−0.90
J0754+2424	07 54 45.52	+24 24 25.3	0.373	PHOT	20.66	−21.33	0.611	0.104	0.044	NRAO	−0.79	−0.69
J0759+1247	07 59 30.94	+12 47 22.8	…	…	…	…	1.444	0.147	0.031	NRAO	−1.02	−1.25
J0800+4957	08 00 06.84	+49 57 55.0	0.396	PHOT	19.65	−22.01	0.400	0.093	…	…	−0.65	…
J0813+3007	08 13 37.78	+30 07 10.6	…	…	23.37	…	0.660	0.107	0.029	NRAO	−0.81	−1.05
J0814+0602[a]	08 14 04.55	+06 02 38.3	0.562	SPEC/Q	19.79	−22.65	1.255	0.219	0.088	NRAO	−0.78	−0.73
J0816+3804	08 16 01.88	+38 04 15.4	0.173	SPEC	16.46	−22.65	1.881	0.427	0.148	NRAO	−0.66	−0.85
J0818+1508	08 18 41.57	+15 08 33.5	0.330	SPEC/Q	18.93	−21.90	0.334	0.065	0.032	NRAO	−0.73	−0.57
J0822+0519	08 22 26.42	+05 19 51.1	0.654	SPEC/Q	19.70	−22.17	3.844	0.343	0.135	NRAO	−1.08	−0.75
J0824+0317	08 24 00.50	+03 17 49.3	0.215	SPEC	17.71	−21.94	0.493	0.134	0.061	NRAO	−0.58	−0.63
J0845+5740	08 45 09.65	+57 40 35.5	0.237	SPEC	18.37	−21.95	0.268	0.047	…	…	−0.77	…
J0852+2620	08 52 36.12	+26 20 13.4	0.477	SPEC	20.70	−21.65	0.329	0.066	…	…	−0.71	…
J0859+0805	08 59 15.19	+08 05 39.7	0.565	SPEC	20.25	−22.95	0.233	0.037	…	…	−0.82	…
J0859+5851	08 59 42.66	+58 51 16.6	0.443	PHOT	19.65	−22.20	0.206	0.039	…	…	−0.74	…
J0859−0252	08 59 54.12	−02 52 41.9	…	…	…	…	2.225	0.395	0.127	PMN	−0.77	−0.91
J0903+5600	09 03 31.03	+56 00 39.9	0.408	PHOT	21.32	−20.16	0.553	0.130	0.060	NRAO	−0.64	−0.62
J0906+0645	09 06 38.35	+06 45 24.6	0.157	PHOT	23.65	−17.60	0.425	0.098	…	…	−0.65	…
J0908+2158	09 08 27.86	+21 58 23.8	…	…	…	…	0.815	0.116	0.033	NRAO	−0.87	−1.01
J0914+0824	09 14 51.07	+08 24 40.1	…	…	…	…	0.378	0.074	…	…	−0.73	…
J0923+3614	09 23 46.43	+36 14 07.3	0.734	PHOT	22.87	−21.84	0.468	0.082	0.028	NRAO	−0.77	−0.86
J0924+4034	09 24 01.16	+40 34 57.2	0.160	SPEC	15.67	−23.21	2.022	0.318	0.102	NRAO	−0.82	−0.91
J0928−0607	09 28 02.68	−06 07 52.6	…	…	…	…	0.779	0.188	0.081	PMN	−0.63	−0.67
J0930+2343[a]	09 30 14.90	+23 43 59.2	0.538	SPEC	19.87	−22.95	1.590	0.303	0.097	NRAO	−0.74	−0.91
J0932+1611[a]	09 32 38.30	+16 11 57.3	0.191	SPEC	17.19	−22.16	…	…	0.193	NRAO	…	…
J0942+0444	09 42 40.45	+04 44 23.1	0.718	PHOT	23.55	−20.90	0.362	0.071	…	…	−0.72	…
J0949+4456	09 49 53.64	+44 56 55.7	0.190	PHOT	18.26	−21.07	0.599	0.207	0.061	NRAO	−0.47	−0.98
J0956−0001	09 56 40.77	−00 01 23.9	0.139	SPEC	16.29	−22.26	0.375	0.097	0.078	NRAO	−0.60	−0.17
J1004+3506	10 04 08.95	+35 06 23.6	0.611	SPEC/Q	20.80	−22.53	0.990	0.174	0.053	NRAO	−0.77	−0.95
J1010+5303	10 10 28.07	+53 03 13.0	0.341	SPEC	18.72	−22.27	0.291	0.050	…	…	−0.78	…
J1011−0607	10 11 34.80	−06 07 53.1	…	…	…	…	0.209	0.033	…	…	−0.82	…
J1017+6329	10 17 32.51	+63 29 53.8	0.184	SPEC	17.28	−21.93	0.765	0.174	0.072	NRAO	−0.66	−0.71
J1031+0443	10 31 18.85	+04 43 07.7	0.672	PHOT	22.89	−20.99	5.945	0.753	0.204	NRAO	−0.92	−1.05
J1033+3530	10 33 58.55	+35 30 07.2	0.611	PHOT	20.91	−22.58	0.405	0.086	…	NRAO	−0.69	…
J1039+3540	10 39 00.86	+35 40 50.1	0.569	SPEC	19.81	−22.91	0.186	0.071	…	…	−0.43	…
J1039+4648	10 39 24.92	+46 48 11.5	0.531	SPEC	19.76	−22.99	0.641	0.121	0.072	NRAO	−0.74	−0.41
J1046−0113	10 46 32.43	−01 13 38.1	0.184	PHOT	18.03	−21.26	0.563	0.132	0.096	NRAO	−0.64	−0.25
J1054+4703	10 54 26.39	+47 03 27.4	0.430	PHOT	20.55	−21.94	0.589	0.101	0.044	NRAO	−0.78	−0.66
J1108+2636	11 08 53.80	+26 36 50.2	…	…	…	…	0.702	0.093	0.065	NRAO	−0.90	−0.28
J1128+1711	11 28 48.72	+17 11 04.5	0.347	SPEC	18.31	−22.72	2.091	0.446	0.127	NRAO	−0.69	−1.01
J1136+0151	11 36 49.98	+01 51 21.3	0.485	PHOT	20.65	−21.63	0.284	0.064	…	…	−0.66	…
J1138+4950	11 38 16.62	+49 50 25.0	0.510	SPEC/Q	20.18	−22.16	0.303	0.072	0.033	NRAO	−0.64	−0.62
J1145+1529	11 45 22.19	+15 29 43.2	0.068	SPEC	14.58	−22.25	1.043	0.350	0.187	NRAO	−0.48	−0.50
J1152+2016	11 52 25.55	+20 16 02.1	0.444	PHOT	20.07	−22.24	0.167	0.055	0.044	NRAO	−0.49	−0.17
J1155+4417[a]	11 55 00.34	+44 17 02.2	0.550	PHOT	19.93	−22.31	0.707	0.112	0.054	NRAO	−0.82	−0.58
J1202−0336	12 02 51.32	−03 36 25.8	0.351	PHOT	19.08	−21.82	1.486	0.267	…	…	−0.76	…
J1225+1633	12 25 50.51	+16 33 43.5	0.656	SPEC	20.66	−22.97	0.774	0.187	0.062	NRAO	−0.63	−0.88
J1257+1228	12 57 21.87	+12 28 20.5	0.208	SPEC	17.64	−21.93	1.616	0.454	0.159	NRAO	−0.56	−0.84
J1259+2032[a]	12 59 00.79	+20 32 48.6	0.580	PHOT	21.34	−21.81	0.348	0.060	…	…	−0.78	…
J1300+3505	13 00 48.34	+35 05 27.3	…	…	…	…	0.672	0.218	0.060	NRAO	−0.50	−1.03
J1302+5119	13 02 58.46	+51 19 43.6	…	…	22.77	…	0.438	0.289	0.122	NRAO	−0.18	−0.69
J1308+2258	13 08 54.25	+22 58 22.3	0.677	SPEC	20.49	−23.41	0.491	0.096	…	…	−0.73	…
J1312+1834	13 12 26.65	+18 34 14.9	0.560	SPEC	20.36	−22.22	0.334	0.057	…	…	−0.79	…

Table 2
(Continued)

Short Name	R.A. (J2000)	Decl. (J2000)	z	Qual.	r	M_R	$S_{i,0.15}$ (Jy)	$S_{i,1.4}$ (Jy)	$S_{i,5}$ (Jy)	Ref.$_{5\ \mathrm{GHz}}$	$\alpha_{0.15}^{1.4}$	$\alpha_{1.4}^{5}$
(1)	(2)	(3)	(4)	(5)	(6)	(7)	(8)	(9)	(10)	(11)	(12)	(13)
J1313+0758	13 13 31.40	+07 58 02.5	0.365	PHOT	20.16	−21.07	0.557	0.106	…	…	−0.74	…
J1323+4115	13 23 24.26	+41 15 15.0	0.296	PHOT	18.77	−21.73	3.857	0.621	0.205	NRAO	−0.81	−0.89
J1324+4334	13 24 04.20	+43 34 07.1	0.338	SPEC/Q	18.32	−22.51	…	0.182	0.088	NRAO	…	−0.58
J1327+2853[a]	13 27 13.87	+28 53 18.1	0.300	PHOT	19.20	−21.27	0.687	0.119	0.065	NRAO	−0.78	−0.48
J1329+1818	13 29 39.95	+18 18 42.0	0.514	SPEC	19.94	−22.84	1.191	0.183	0.069	NRAO	−0.83	−0.78
J1330+0248[a]	13 30 51.04	+02 48 43.1	0.623	SPEC	20.62	−22.86	0.477	0.130	…	…	−0.58	…
J1336+4313	13 36 36.06	+43 13 29.0	…	…	…	…	1.643	0.272	0.094	NRAO	−0.80	−0.85
J1340+3749	13 40 51.19	+37 49 11.7	0.218	PHOT	18.87	−20.84	0.276	0.054	0.055	NRAO	−0.73	0.01
J1340+5035[a]	13 40 02.96	+50 35 39.7	0.232	SPEC	18.35	−21.56	0.146	0.096	…	NRAO	−0.18	…
J1343+1933	13 43 53.97	+19 33 34.1	0.513	PHOT	21.64	−21.25	0.848	0.123	0.045	NRAO	−0.86	−0.80
J1355+0940	13 55 18.04	+09 40 22.9	0.619	PHOT	21.20	−22.50	2.746	0.435	0.170	NRAO	−0.82	−0.75
J1403+4953	14 03 49.79	+49 53 05.4	0.491	SPEC	20.76	−21.63	0.393	0.099	…	…	−0.61	…
J1407+2722	14 07 42.26	+27 22 07.6	0.235	SPEC	18.31	−22.38	0.167	0.053	…	…	−0.51	…
J1417+2019	14 17 02.13	+20 19 03.3	0.535	PHOT	20.57	−22.08	0.374	0.071	…	…	−0.74	…
J1426+2712[a]	14 26 46.41	+27 12 23.6	0.677	PHOT	22.15	−21.86	0.711	0.155	0.053	NRAO	−0.68	−0.86
J1437+3519	14 37 56.45	+35 19 37.1	0.537	SPEC/Q	18.53	−22.87	0.268	0.096	0.064	NRAO	−0.45	−0.32
J1445−0130	14 45 47.33	−01 30 45.7	0.610	PHOT	22.35	−21.29	1.307	0.185	…	…	−0.87	…
J1500−0450	15 00 16.24	−04 50 36.6	…	…	…	…	1.807	0.310	…	…	−0.78	…
J1506+0740	15 06 36.54	+07 40 16.9	0.684	PHOT	21.99	−21.95	0.145	0.026	…	…	−0.76	…
J1508+6137	15 08 16.29	+61 37 56.3	0.385	PHOT	22.09	−19.53	0.306	0.053	…	…	−0.78	…
J1508−0730	15 08 55.22	−07 30 36.4	…	…	…	…	0.265	0.080	…	…	−0.53	…
J1509+2124	15 09 04.13	+21 24 15.1	0.311	SPEC	18.52	−22.30	0.613	0.149	0.060	NRAO	−0.63	−0.73
J1511+0455	15 11 49.30	+04 55 36.1	0.893	PHOT	21.60	−23.66	0.446	0.081	…	…	−0.76	…
J1517+2122	15 17 04.61	+21 22 42.1	0.349	PHOT	19.16	−21.91	1.405	0.243	0.107	NRAO	−0.78	−0.66
J1522−0504	15 22 45.38	−05 04 04.3	…	…	…	…	7.124	1.184	0.361	PMN	−0.80	−0.95
J1542+1214	15 42 02.85	+12 14 27.6	…	…	…	…	0.404	0.063	…	…	−0.83	…
J1544+3044[a]	15 44 13.39	+30 44 01.1	0.599	PHOT	21.99	−21.23	1.126	0.239	0.093	NRAO	−0.69	−0.75
J1547+2130	15 47 19.43	+21 30 12.0	…	…	…	…	0.196	0.046	0.043	NRAO	−0.64	−0.05
J1548+0149	15 48 42.66	+01 49 19.4	0.609	PHOT	20.99	−23.25	0.772	0.132	…	…	−0.79	…
J1554+3811	15 54 16.04	+38 11 32.5	0.194	SPEC/Q	20.77	−18.89	0.265	0.061	…	…	−0.65	…
J1608+0122	16 08 33.28	+01 22 31.0	…	…	…	…	0.299	0.024	…	…	−1.12	…
J1608+2945	16 08 09.55	+29 45 14.9	0.226	SPEC	18.74	−21.15	0.198	0.060	…	…	−0.53	…
J1622+0707	16 22 45.42	+07 07 14.6	0.597	SPEC/Q	20.01	−23.18	0.748	0.163	0.067	NRAO	−0.68	−0.71
J1648+2604	16 48 57.36	+26 04 41.2	0.137	SPEC	17.88	−20.81	0.456	0.145	0.090	NRAO	−0.51	−0.38
J1715+4938	17 15 47.52	+49 38 40.2	…	…	…	…	0.657	0.091	…	…	−0.88	…
J2028+0035	20 28 55.27	+00 35 12.6	0.192	PHOT	17.51	−22.03	1.453	0.382	0.145	NRAO	−0.59	−0.77
J2034+0052	20 34 59.54	+00 52 21.4	0.321	PHOT	19.25	−21.85	0.332	0.054	…	…	−0.81	…
J2058+0311	20 58 23.53	+03 11 24.4	…	…	…	…	0.708	0.268	0.095	NRAO	−0.43	−0.83
J2100−0335	21 00 53.62	−03 35 16.6	…	…	…	…	2.065	0.349	0.135	PMN	−0.79	−0.76
J2147−0359	21 47 31.06	−03 59 42.4	0.612	PHOT	20.73	−22.55	0.530	0.135	…	…	−0.61	…
J2228−0653	22 28 02.33	−06 53 54.8	0.629	PHOT	21.38	−22.51	0.581	0.127	…	…	−0.68	…
J2236+0427	22 36 28.89	+04 27 51.8	0.303	SPEC	18.29	−22.62	1.638	0.442	0.130	NRAO	−0.58	−0.98
J2320−0753	23 20 20.30	−07 53 19.3	0.390	PHOT	20.19	−21.32	0.262	0.049	…	…	−0.75	…
J2332+0247	23 32 59.28	+02 47 15.3	0.197	PHOT	17.88	−21.68	0.663	0.247	0.121	NRAO	−0.44	−0.57

Note.
Column (1): short name. Column (2): R.A. (J2000, hh:mm:ss). Column (3): decl. (J2000, dd:mm:ss). Column (4): redshift. Column (5): redshift quality flag. PHOT: photometric redshift; SPEC: spectroscopic redshift; SPEC/Q: quasar. Column (6): apparent r-band magnitude of the host galaxy. Column (7): absolute R-band magnitude of the host galaxy. Column (8): integrated 150 MHz flux density (Jy; the uncertainty is 10% of the total flux density). Column (9): integrated 1.4 GHz flux density (Jy; the uncertainty is 3% of the total flux density). Column (10): integrated 5 GHz/4.85 GHz flux density (Jy). Column (11): references for 5 GHz/4.85 GHz flux density. NRAO: NRAO Green Bank 300 Foot 4.85 GHz survey; PMN: the Parkes-MIT-NRAO 4.85 GHz Surveys; MIT-GB: the MIT-Green Bank 5 GHz Survey. Column (12): spectral index between 150 MHz and 1.4 GHz. Column (13): spectral index between 1.4 GHz and 5 GHz/4.85 GHz.
[a] Also appeared in Proctor (2011).

J0710+3546, which is not covered in that survey. The center of each image coincides with the above-estimated most plausible position of the host galaxy. Interestingly, a radio core is detected in only ∼10 of our strong XRGs.

Spectroscopic or, alternatively, photometric redshifts were taken from the NED and/or SDSS databases. Spectroscopic redshifts could be found for 41 (∼39%) of our 106 "strong" XRG candidates and 61 (∼33%) of our 184 "probable" XRG candidates. For the remaining "strong" candidates, photometric redshifts were taken from the SDSS archive; these are based on the SDSS phototree method. In Tables 2 and 3 we list the redshift values (Column (4)) marked as "SPEC" and "PHOT " for the spectroscopic and photometric redshifts (Column (5)), SDSS r-band apparent magnitude (Column (6)), and the

Table 3
"Probable" X-shaped Radio Source Candidates

Short Name	R.A. (J2000)	Decl. (J2000)	z	Qual.	r	M_R	$S_{i,0.15}$ (Jy)	$S_{i,1.4}$ (Jy)	$S_{i,5}$ (Jy)	Ref.$_{5\ \mathrm{GHz}}$
(1)	(2)	(3)	(4)	(5)	(6)	(7)	(8)	(9)	(10)	(11)
J0009+0457	00 09 18.92	+04 57 53.2	0.545	PHOT	21.20	−21.55	1.402	0.320	0.094	NRAO
J0028−0428	00 28 15.26	−04 28 55.3	0.267	SPEC	17.51	−22.84	0.484	0.092	0.063	PMN
J0031−0421	00 31 41.91	−04 21 56.0	0.485	SPEC	21.05	−21.56	0.133	0.066	…	…
J0049−0507	00 49 55.56	−05 07 04.3	…	…	22.40	…	0.596	0.152	0.064	PMN
J0051+0728	00 51 27.90	+07 28 56.5	0.512	PHOT	20.13	−22.71	4.058	0.506	0.153	NRAO
J0055−0829	00 55 51.49	−08 29 53.8	0.705	SPEC	21.11	−23.04	1.495	0.337	0.112	PMN
J0125+0617	01 25 25.82	+06 17 31.5	0.274	PHOT	18.81	−21.57	1.875	0.423	0.161	NRAO
J0131+0314	01 31 05.68	+03 14 52.6	0.468	PHOT	20.48	−21.68	0.846	0.182	0.059	NRAO
J0138−0654	01 38 19.05	−06 54 58.0	…	…	…	…	0.604	0.200	0.151	PMN
J0158+1150	01 58 46.34	+11 50 54.6	0.535	SPEC	19.71	−23.33	1.292	0.219	0.069	NRAO
J0213+0518	02 13 36.30	+05 18 18.9	0.340	PHOT	23.87	−17.58	2.423	0.376	0.104	NRAO
J0214+0042	02 14 37.24	+00 42 35.3	0.290	SPEC	18.20	−22.38	0.501	0.131	0.057	NRAO
J0219+0155	02 19 58.74	+01 55 48.9	0.041	SPEC	13.70	−20.79	2.062	0.560	0.228	NRAO
J0227+0258	02 27 07.49	+02 58 11.4	0.692	PHOT	22.35	−22.54	0.750	0.126	…	…
J0227−1114	02 27 23.92	−11 14 43.3	…	…	…	…	0.862	0.194	…	…
J0234+0248	02 34 26.37	+02 48 32.3	0.586	SPEC	20.57	−22.69	0.594	0.119	0.041	PMN
J0249−0414	02 49 17.36	−04 14 10.0	0.313	SPEC	20.82	−20.79	1.081	0.266	0.126	PMN
J0256+0026	02 56 29.62	+00 26 30.9	…	…	…	…	0.289	0.044	…	…
J0304−0015	03 04 43.84	−00 15 11.1	0.264	SPEC/Q	19.14	−21.19	…	0.046	0.048	PMN
J0310+0555	03 10 23.02	+05 55 52.7	0.582	PHOT	20.46	−22.96	1.041	0.200	0.066	NRAO
J0328−0639	03 28 30.43	−06 39 53.8	…	…	…	…	1.005	0.118	…	…
J0654+5903	06 54 32.41	+59 03 36.0	…	…	…	…	1.158	0.221	0.086	NRAO
J0713+4849	07 13 27.96	+48 49 24.9	…	…	…	…	4.715	0.540	0.137	NRAO
J0722+4307	07 22 19.44	+43 07 18.3	…	…	14.80	…	0.423	0.104	0.035	NRAO
J0724+3620	07 24 23.22	+36 20 32.2	…	…	…	…	0.339	0.145	0.067	MIT-GB
J0726+5104	07 26 45.57	+51 04 07.0	…	…	…	…	0.338	0.113	0.068	NRAO
J0729+4938	07 29 16.16	+49 38 53.8	…	…	…	…	1.219	0.187	0.064	NRAO
J0738+4601	07 38 18.38	+46 01 28.3	0.431	SPEC	20.14	−21.89	1.873	0.242	0.147	NRAO
J0741+3333	07 41 25.22	+33 33 19.9	0.364	SPEC/Q	17.20	−23.42	…	0.107	0.157	NRAO
J0741+4618	07 41 01.81	+46 18 39.3	…	…	…	…	1.227	0.228	0.058	NRAO
J0749+5353	07 49 21.21	+53 53 47.3	…	…	…	…	3.699	0.439	0.127	NRAO
J0750+2825	07 50 01.81	+28 25 09.9	0.531	PHOT	20.01	−22.75	5.258	0.765	0.273	NRAO
J0801+4350	08 01 07.89	+43 50 30.4	0.255	SPEC	17.15	−23.06	0.348	0.077	0.027	NRAO
J0803+3056	08 03 33.15	+30 56 40.3	0.565	SPEC	20.89	−22.41	3.183	0.298	0.077	NRAO
J0811+5010[a]	08 11 17.07	+50 10 18.9	0.327	PHOT	22.80	−18.89	3.868	0.534	0.156	NRAO
J0813+2655	08 13 43.61	+26 55 09.8	0.325	SPEC	17.57	−23.32	0.489	0.074	…	…
J0816+5224	08 16 24.74	+52 24 46.1	0.689	PHOT	20.81	−22.47	0.577	0.083	0.048	NRAO
J0817+0708	08 17 16.15	+07 08 46.2	0.262	SPEC	18.72	−21.55	…	0.170	0.078	NRAO
J0818+2006	08 18 54.88	+20 06 20.9	0.075	SPEC	15.64	−21.44	0.578	0.144	0.061	NRAO
J0821+1702[a]	08 21 14.65	+17 02 09.1	0.986	PHOT	23.11	−22.69	…	…	0.069	NRAO
J0823+5812[a]	08 23 33.47	+58 12 11.0	0.778	SPEC/Q	18.51	−23.78	0.722	0.067	0.045	NRAO
J0831+3048	08 31 36.99	+30 48 26.9	0.999	SPEC/Q	18.72	−24.39	…	0.156	0.059	NRAO
J0832+4301	08 32 42.55	+43 01 51.1	0.357	PHOT	21.00	−20.32	0.239	0.059	…	…
J0837+4450[a]	08 37 52.75	+44 50 25.8	0.206	SPEC/Q	17.14	−22.44	8.641	0.934	0.538	NRAO
J0843+1700	08 43 07.49	+17 00 21.9	0.510	SPEC/Q	20.06	−22.42	0.545	0.117	0.044	NRAO
J0844+4008	08 44 55.89	+40 08 13.8	0.527	SPEC	19.79	−22.80	2.515	0.409	0.139	NRAO
J0845+5002[a]	08 45 43.07	+50 02 42.6	0.465	PHOT	20.51	−22.18	0.577	0.079	…	…
J0851+4859	08 51 25.05	+48 59 35.7	0.489	SPEC	19.78	−22.73	…	0.330	0.166	NRAO
J0852+5913	08 52 31.34	+59 13 50.4	0.445	PHOT	20.35	−21.91	0.841	0.166	0.051	NRAO
J0855+5239	08 55 14.67	+52 39 05.1	0.354	PHOT	18.71	−22.50	3.566	0.439	0.147	NRAO
J0856+0905	08 56 32.39	+09 05 37.6	…	…	…	…	1.426	0.163	0.041	PMN
J0858+0804	08 58 30.61	+08 04 22.7	0.455	SPEC/Q	18.62	−22.87	1.235	0.136	0.115	NRAO
J0859+1845	08 59 43.84	+18 45 46.8	0.322	PHOT	19.25	−21.59	0.735	0.237	0.085	NRAO
J0901−0555	09 01 46.78	−05 55 04.0	…	…	…	…	…	0.336	0.148	PMN
J0904+1454	09 04 17.99	+14 54 30.5	…	…	…	…	0.363	0.064	…	…
J0904+1532	09 04 10.07	+15 32 09.5	0.426	SPEC/Q	19.35	−22.51	0.795	0.150	…	…
J0906−0746	09 06 17.83	−07 46 03.6	…	…	…	…	1.960	0.260	0.082	PMN
J0907+4128	09 07 51.47	+41 28 14.1	…	…	…	-	1.100	0.202	0.065	NRAO
J0909+0119	09 09 37.69	+01 19 41.3	0.659	PHOT	22.55	−21.79	0.551	0.132	…	…
J0909+0326	09 09 37.36	+03 26 57.7	0.757	PHOT	22.39	−22.60	1.447	0.236	0.064	NRAO
J0910−0420	09 10 46.20	−04 20 06.5	…	…	…	…	2.046	0.340	…	NRAO

Table 3
(Continued)

Short Name	R.A. (J2000)	Decl. (J2000)	z	Qual.	r	M_R	$S_{i,0.15}$ (Jy)	$S_{i,1.4}$ (Jy)	$S_{i,5}$ (Jy)	Ref.$_{5\ \mathrm{GHz}}$
(1)	(2)	(3)	(4)	(5)	(6)	(7)	(8)	(9)	(10)	(11)
J0911+3724	09 11 53.61	+37 24 13.4	0.104	SPEC	14.71	−23.08	2.351	0.669	0.299	NRAO
J0915+4524	09 15 53.59	+45 24 10.4	…	…	…	…	0.275	0.113	0.033	NRAO
J0920+0750	09 20 02.10	+07 50 01.8	0.553	SPEC	20.42	−22.64	0.098	0.037	…	…
J0921+1523	09 21 44.36	+15 23 58.3	0.484	PHOT	20.24	−22.06	1.029	0.167	0.063	NRAO
J0921+5744	09 21 12.79	+57 44 14.7	0.197	PHOT	17.62	−21.85	0.342	0.078	0.021	NRAO
J0926+4652	09 26 39.77	+46 52 52.3	0.808	PHOT	22.61	−21.87	…	0.065	0.064	NRAO
J0929+3121	09 29 54.13	+31 21 28.3	0.572	PHOT	20.34	−22.18	1.226	0.213	0.078	NRAO
J0937−0214	09 37 07.94	−02 14 26.4	…	…	23.72	…	…	0.049	…	…
J0948+1722[a]	09 48 58.83	+17 22 53.2	0.952	PHOT	22.91	−23.00	0.451	0.089	…	NRAO
J0952+4059	09 52 25.77	+40 59 35.5	0.469	SPEC	20.13	−22.18	0.353	0.074	…	NRAO
J0957+1606	09 57 28.27	+16 06 53.0	…	…	…	…	3.381	0.628	0.205	NRAO
J0957+4847	09 57 53.17	+48 47 18.1	…	…	…	…	1.411	0.176	0.065	NRAO
J0958−0804	09 58 33.25	−08 04 11.4	…	…	…	…	0.140	0.054	…	…
J0959−0601	09 59 32.16	−06 01 36.3	…	…	…	…	5.455	0.434	0.103	PMN
J1009+0529	10 09 43.55	+05 29 53.9	0.942	SPEC/Q	16.92	−25.93	1.151	0.179	0.052	NRAO
J1010+5931	10 10 23.96	+59 31 59.8	0.743	PHOT	21.14	−22.34	1.284	0.180	0.053	NRAO
J1014−0004	10 14 44.32	−00 04 17.3	0.605	PHOT	21.40	−22.08	0.950	0.234	0.102	NRAO
J1018+1058	10 18 04.91	+10 58 44.6	0.453	SPEC	19.47	−22.85	0.186	0.042	…	…
J1019+1134	10 19 02.12	+11 34 33.7	0.780	PHOT	22.22	−21.63	0.217	0.047	…	…
J1021+1443	10 21 56.67	+14 43 31.4	0.111	SPEC	15.95	−22.05	0.824	0.248	0.188	NRAO
J1022+5726	10 22 14.52	+57 26 42.8	0.354	PHOT	19.52	−21.65	0.380	0.082	0.029	NRAO
J1027+4445	10 27 04.63	+44 45 50.2	0.586	SPEC	20.42	−22.86	1.164	0.200	0.060	NRAO
J1032−0449	10 32 40.59	−04 49 38.8	…	…	…	…	0.360	0.084	…	…
J1034+0533	10 34 43.26	+05 33 19.7	0.141	SPEC	15.84	−22.73	0.690	0.186	0.079	NRAO
J1037−0128	10 37 40.99	−01 28 00.6	0.406	PHOT	19.83	−21.87	0.347	0.080	…	…
J1044+3540	10 44 54.87	+35 40 55.0	0.163	SPEC	16.52	−22.37	0.478	0.108	0.043	NRAO
J1047+3544	10 47 11.10	+35 44 37.3	0.380	SPEC	20.49	−20.85	0.147	0.072	0.035	NRAO
J1054+1431	10 54 32.17	+14 31 46.6	0.488	SPEC/Q	19.76	−22.27	3.382	0.600	0.195	NRAO
J1054−0209	10 54 03.24	−02 09 14.0	0.238	PHOT	18.13	−21.89	1.215	0.291	…	…
J1102+0459	11 02 46.28	+04 59 14.1	…	…	…	…	1.637	0.292	0.131	NRAO
J1102+3540	11 02 13.17	+35 40 53.7	0.516	SPEC	20.24	−22.35	1.042	0.158	0.051	NRAO
J1104+2828	11 04 33.40	+28 28 43.1	0.214	SPEC	17.46	−22.23	0.190	0.040	0.088	NRAO
J1104+3243	11 04 38.59	+32 43 30.0	0.458	SPEC	20.07	−22.09	1.149	0.198	0.059	NRAO
J1104+6416	11 04 02.06	+64 16 12.7	0.460	SPEC	19.59	−22.46	0.747	0.149	0.067	NRAO
J1107+1134	11 07 02.51	+11 34 45.9	0.538	PHOT	21.79	−20.28	2.219	0.299	0.090	NRAO
J1114+3022	11 14 55.13	+30 22 41.1	0.308	SPEC	18.82	−21.85	0.369	0.028	…	…
J1114+4133[a]	11 14 25.86	+41 33 15.8	0.515	PHOT	21.87	−21.15	1.028	0.211	0.082	NRAO
J1115+3302	11 15 09.94	+33 02 44.9	0.438	PHOT	19.70	−22.17	1.128	0.248	0.091	NRAO
J1116+4516	11 16 54.15	+45 16 17.4	0.112	SPEC	16.01	−21.90	0.275	0.060	…	…
J1128+5832	11 28 29.51	+58 32 02.7	0.508	PHOT	19.85	−22.50	1.773	0.149	…	…
J1130−0329	11 30 09.44	−03 29 38.7	0.531	PHOT	20.45	−22.57	3.979	0.645	0.220	PMN
J1132+1001	11 32 41.91	+10 01 15.6	0.524	SPEC	19.43	−23.37	0.204	0.045	…	…
J1134+2424	11 34 00.18	+24 24 23.7	0.362	PHOT	19.55	−21.68	0.247	0.049	0.064	NRAO
J1134+3046	11 34 19.26	+30 46 38.4	0.246	SPEC	17.72	−22.32	0.532	0.155	0.157	NRAO
J1137+3709[a]	11 37 53.02	+37 09 13.3	0.388	PHOT	19.80	−22.18	0.876	0.208	0.071	NRAO
J1139+4507	11 39 52.06	+45 07 16.2	…	…	…	…	0.421	0.054	…	NRAO
J1139+5312	11 39 56.83	+53 12 11.8	0.327	PHOT	18.92	−21.92	0.916	0.188	0.070	NRAO
J1140+1743	11 40 16.93	+17 43 40.8	0.012	SPEC	12.17	−20.63	3.884	1.143	0.635	NRAO
J1140−0519	11 40 54.34	−05 19 43.7	…	…	…	…	0.332	0.059	…	…
J1141−0347	11 41 26.09	−03 47 08.9	0.695	PHOT	21.76	−22.55	1.175	0.145	…	…
J1142+5800	11 42 15.26	+58 00 01.9	0.574	PHOT	21.20	−21.66	0.444	0.074	…	…
J1143+3328	11 43 43.74	+33 28 52.3	0.689	PHOT	21.26	−22.19	0.958	0.146	0.035	NRAO
J1146+2643	11 46 42.68	+26 43 20.5	0.503	PHOT	21.91	−21.31	0.468	0.085	0.041	NRAO
J1151−0518[a]	11 51 12.65	−05 18 16.2	…	…	…	…	…	0.224	0.111	PMN
J1152−0005	11 52 19.52	−00 05 23.9	…	…	18.67	…	0.467	0.095	0.042	PMN
J1156+2138	11 56 45.31	+21 38 08.8	0.622	SPEC	20.98	−23.55	1.003	0.198	0.075	NRAO
J1156+4115	11 56 43.80	+41 15 28.5	0.163	SPEC	17.75	−21.15	0.141	0.044	…	…
J1201+3257	12 01 51.92	+32 57 00.6	…	…	…	…	0.198	0.154	0.070	NRAO
J1206+2215	12 06 33.35	+22 15 37.6	0.065	SPEC	14.09	−22.59	4.236	0.749	0.394	NRAO
J1206+3740	12 06 32.55	+37 40 24.8	0.344	SPEC	18.45	−22.60	0.402	0.081	…	…

Table 3
(Continued)

Short Name	R.A. (J2000)	Decl. (J2000)	z	Qual.	r	M_R	$S_{i,0.15}$ (Jy)	$S_{i,1.4}$ (Jy)	$S_{i,5}$ (Jy)	Ref.$_{5\ \mathrm{GHz}}$
(1)	(2)	(3)	(4)	(5)	(6)	(7)	(8)	(9)	(10)	(11)
J1211+5717	12 11 22.95	+57 17 52.8	0.730	PHOT	21.80	−22.50	1.998	0.215	0.055	NRAO
J1212+6140	12 12 13.14	+61 40 01.1	…	…	…	…	1.717	0.290	0.102	NRAO
J1225+0051	12 25 11.81	+00 51 52.6	0.575	PHOT	21.61	−22.12	0.281	0.065	…	…
J1240−0023	12 40 08.27	−00 23 40.7	0.343	PHOT	19.83	−21.22	0.396	0.094	…	NRAO
J1243+6404	12 43 16.02	+64 04 25.3	…	…	21.56	…	1.961	0.241	0.064	NRAO
J1246+1710	12 46 24.32	+17 10 52.6	0.702	SPEC	20.93	−23.07	1.559	0.240	0.055	NRAO
J1247+1947	12 47 16.71	+19 47 50.4	0.432	SPEC/Q	19.47	−22.35	1.218	0.219	0.084	NRAO
J1251+0856	12 51 42.87	+08 56 17.0	0.300	PHOT	18.26	−22.15	8.371	0.852	0.547	NRAO
J1259+0125	12 59 16.82	+01 25 42.7	0.713	SPEC	20.78	−23.31	0.948	0.204	…	…
J1259+1443	12 59 18.07	+14 43 25.9	0.622	PHOT	20.90	−22.83	1.457	0.231	0.072	NRAO
J1301+1041[a]	13 01 16.13	+10 41 38.6	0.616	PHOT	22.04	−21.67	0.571	0.169	0.053	NRAO
J1303+0609	13 03 07.09	+06 09 07.7	0.445	PHOT	22.56	−19.90	0.385	0.066	…	…
J1305−0013	13 05 40.14	−00 13 46.6	…	…	20.86	…	0.563	0.118	…	…
J1306+4257	13 06 52.38	+42 57 02.0	0.657	SPEC	21.29	−21.67	0.737	0.145	0.045	NRAO
J1310+4644	13 10 42.38	+46 44 35.0	…	…	…	…	0.458	0.044	…	…
J1314−0143	13 14 34.45	−01 43 39.2	0.220	SPEC	17.56	−22.19	0.198	0.105	…	…
J1324+1801	13 24 28.14	+18 01 24.7	…	…	…	…	…	0.111	0.060	MIT-GB
J1326+3647	13 26 02.39	+36 47 59.3	0.054	SPEC	14.64	−21.59	3.762	1.019	0.475	NRAO
J1334+4056	13 34 54.38	+40 56 54.7	0.238	SPEC	16.62	−23.31	0.855	0.192	0.060	NRAO
J1336+1611	13 36 32.19	+16 11 07.0	1.395	PHOT	20.00	−24.48	1.303	0.122	0.039	NRAO
J1347+1048	13 47 15.88	+10 48 24.9	0.670	PHOT	23.76	−20.39	0.213	0.049	…	…
J1348−0621	13 48 06.52	−06 21 28.7	…	…	…	…	1.203	0.247	…	…
J1351−0549	13 51 19.82	−05 49 25.1	0.557	PHOT	22.64	−20.57	…	0.965	…	…
J1353+2809	13 53 08.34	+28 09 08.8	0.466	PHOT	19.89	−21.73	…	0.168	0.132	NRAO
J1358+4008	13 58 08.16	+40 08 59.1	…	…	…	…	0.294	0.049	…	…
J1359+2954	13 59 06.20	+29 54 30.9	…	…	…	…	0.155	0.037	…	…
J1419+2600	14 19 40.53	+26 00 14.9	0.465	PHOT	20.78	−21.68	0.351	0.073	0.032	NRAO
J1427+3247	14 27 58.73	+32 47 41.5	0.570	SPEC/Q	18.47	−23.00	0.540	0.050	0.076	NRAO
J1434+4251	14 34 22.22	+42 51 33.0	0.451	PHOT	21.03	−20.93	0.562	0.100	0.042	NRAO
J1442+2808	14 42 14.55	+28 08 21.5	0.280	PHOT	18.69	−21.80	0.395	0.155	0.077	NRAO
J1446+0728	14 46 31.52	+07 28 59.8	0.742	SPEC/Q	21.20	−22.98	4.709	0.574	0.191	NRAO
J1447+1221	14 47 43.60	+12 21 08.4	0.150	PHOT	17.83	−20.91	0.593	0.190	0.073	NRAO
J1457+3055	14 57 38.15	+30 55 35.5	0.564	SPEC/Q	20.64	−22.31	0.595	0.143	0.055	NRAO
J1501−0751	15 01 20.36	−07 51 06.4	0.208	PHOT	18.05	−21.39	1.066	0.277	…	…
J1506−0046	15 06 51.23	−00 46 29.4	…	…	…	…	0.240	0.097	…	…
J1522+1012	15 22 17.25	+10 12 58.6	0.267	PHOT	18.88	−21.45	1.257	0.333	0.148	NRAO
J1526−0337	15 26 32.26	−03 37 47.3	…	…	…	…	1.795	0.352	0.106	PMN
J1528+1323	15 28 06.64	+13 23 45.9	0.675	SPEC/Q	18.22	−24.04	1.424	0.225	0.059	NRAO
J1540+4602	15 40 09.75	+46 02 20.1	0.201	PHOT	20.32	−18.96	0.223	0.047	…	…
J1541+2151	15 41 06.47	+21 51 49.2	0.721	SPEC/Q	20.70	−22.03	0.650	0.105	0.043	NRAO
J1544+0802[a]	15 44 48.84	+08 02 02.4	0.536	PHOT	21.11	−21.92	0.753	0.178	0.067	NRAO
J1548+4451	15 48 17.19	+44 51 47.4	0.599	PHOT	21.33	−22.39	0.128	0.116	0.030	NRAO
J1553+2957	15 53 49.79	+29 57 26.8	0.590	PHOT	21.76	−22.30	0.264	0.082	…	…
J1600−0144	16 00 29.65	−01 44 44.6	…	…	…	…	2.600	0.340	0.136	NRAO
J1601+3056	16 01 27.96	+30 56 01.7	…	…	17.89	…	0.203	0.086	…	…
J1601+3132	16 01 58.11	+31 32 25.1	0.545	PHOT	21.49	−21.66	0.803	0.136	0.038	NRAO
J1611+2207	16 11 03.95	+22 07 19.6	0.282	PHOT	19.01	−21.78	1.895	0.193	0.099	NRAO
J1618+1639	16 18 49.91	+16 39 44.5	…	…	…	…	1.136	0.191	0.045	NRAO
J1623+2351	16 23 05.81	+23 51 34.9	0.429	SPEC	20.24	−21.67	1.375	0.305	0.112	NRAO
J1647+2251	16 47 26.30	+22 51 58.0	0.917	PHOT	22.86	−22.32	0.281	0.069	…	…
J1711+2414	17 11 12.49	+24 14 56.6	…	…	…	…	1.067	0.285	0.062	NRAO
J1730+3816[a]	17 30 44.26	+38 16 29.1	…	…	…	…	2.558	0.649	0.244	NRAO
J2020+0012	20 20 34.91	+00 12 28.2	0.134	PHOT	17.61	−21.08	1.351	0.342	0.171	NRAO
J2114+0753	21 14 34.58	+07 53 02.0	0.134	PHOT	17.31	−21.25	0.877	0.383	0.192	NRAO
J2125−0534	21 25 53.84	−05 34 23.6	0.114	PHOT	21.10	−16.90	0.618	0.368	0.145	PMN
J2151+1219	21 51 03.88	+12 19 53.6	…	…	…	…	6.904	0.929	0.238	NRAO
J2233+0317	22 33 48.71	+03 17 41.7	0.359	PHOT	19.86	−21.47	0.674	0.190	0.050	NRAO
J2239−0429	22 39 32.79	−04 29 32.3	0.560	PHOT	20.11	−23.04	9.107	0.554	0.070	PMN
J2240−0435	22 40 29.92	−04 35 57.3	0.251	PHOT	18.54	−21.66	1.336	0.159	0.121	PMN
J2254−0010	22 54 05.31	−00 10 33.1	…	…	…	…	1.040	0.215	0.066	NRAO

Table 3
(Continued)

Short Name	R.A. (J2000)	Decl. (J2000)	z	Qual.	r	M_R	$S_{i,0.15}$ (Jy)	$S_{i,1.4}$ (Jy)	$S_{i,5}$ (Jy)	Ref.$_{5\ \mathrm{GHz}}$
(1)	(2)	(3)	(4)	(5)	(6)	(7)	(8)	(9)	(10)	(11)
J2300+0810	23 00 16.10	+08 10 37.4	0.162	PHOT	15.92	−23.19	1.519	0.408	0.184	NRAO
J2320+0257	23 20 46.29	+02 57 06.5	0.405	PHOT	22.06	−20.67	4.815	0.489	0.222	NRAO
J2351−0402	23 51 27.28	−04 02 22.5	…	…	20.89	…	…	0.353	0.171	PMN

Note.
Column (1): short name. Column (2): R.A. (J2000, hh:mm:ss). Column (3): decl. (J2000, dd:mm:ss). Column (4): redshift. Column (5): redshift quality flag. PHOT: photometric redshift; SPEC: spectroscopic redshift; SPEC/Q: quasar. Column (6): apparent r-band magnitude of the host galaxy. Column (7): absolute R-band magnitude of the host galaxy. Column (8): integrated 150 MHz flux density (Jy; the uncertainty is 10% of the total flux density). Column (9): integrated 1.4 GHz flux density (Jy; the uncertainty is 3% of the total flux density). Column (10): integrated 5 GHz/4.85 GHz flux density (Jy). Column (11): references for 5 GHz/4.85 GHz flux density. NRAO: NRAO Green Bank 300 Foot 4.85 GHz survey; PMN: the Parkes-MIT-NRAO 4.85 GHz Surveys; MIT-GB: the MIT-Green Bank 5 GHz Survey.
[a] Also appeared in Proctor (2011).

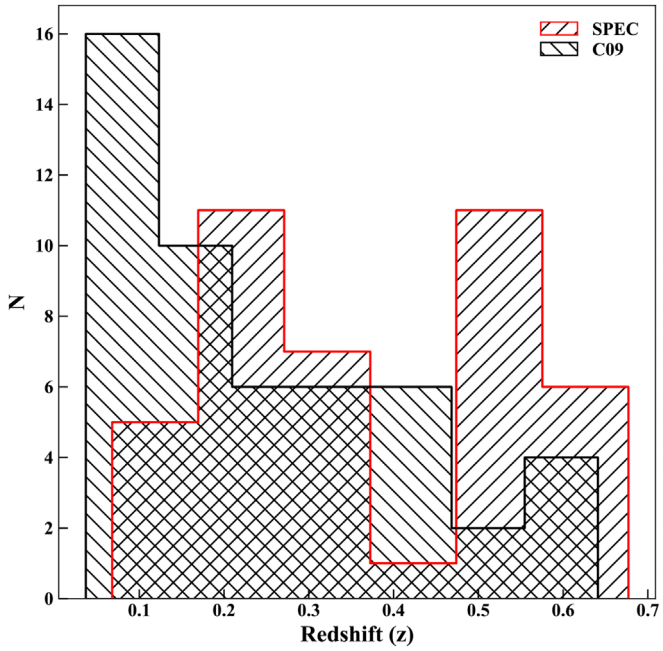

Figure 3. Distributions of spectroscopically measured redshifts available for the 40 strong candidates in the present XRG catalog (SPEC, red-lined histogram) and for the 50 XRGs from C09 (black-lined histogram).

corresponding absolute magnitude (Column (7)) for our 106 "strong" and 184 "probable" XRG candidates, respectively. Figure 3 compares the histograms of spectroscopic redshifts for our strong XRG candidates and for the 50 XRGs from Cheung et al. (2009). It is evident that our strong XRGs are systematically more distant and span a larger range in redshift (from ∼0.06 to ∼0.7, with a median redshift $z \sim 0.37$), as compared to the 50 XRGs in C09, for which the median redshift is $z \sim 0.25$. This difference is not unexpected, given that our selection procedure admits sources of smaller radio (angular) extent (Section 3).

The R-band absolute magnitudes (M_R) of our XRG candidates were computed from the SDSS r-band apparent magnitudes, by applying the k-correction from Blanton & Roweis (2007). The average M_R of our 41 spectroscopically identified "strong" XRG candidates is found to be −22.3, with an rms scatter of 0.8. It is interesting that these XRG candidates with spectroscopic redshifts contain nine quasars (marked as "SPEC/Q" in Column (5) of Table 2). It may be mentioned that X-shaped quasars are known to be quite rare; the first one was reported by Wang et al. (2003) (4C+01.30 at $z = 0.132$). Subsequently, one more X-shaped quasar, WGA J2347+0852, was reported by Landt et al. (2006). In C07, four quasars were identified among their 36 spectroscopically identified XRG candidates. Recently, Saripalli & Roberts (2018) have confirmed a total of 12 quasars in the C07 sample. It may also be noted that just one X-shaped quasar (4C+01.30) is reported to exhibit a double-peaked (broad) emission line system (Zhang et al. 2007). The present catalog of XRG candidates contains another three such rare objects showing double-peaked narrow emission lines: the quasars J0818+1508 and J1554+3811 belong to the "strong" XRGs (Table 2), while J1247+1948 is a "probable" XRG candidate (see Table 3). Since the presence of double-peaked emission lines in X-shaped radio sources may be taken as a clue favoring the binary/dual black hole model (e.g., Lal et al. 2008; Lal et al. 2019), such rare objects are good candidates for confirming an SMBH pair/binary, via high-resolution VLBI. A more detailed analysis of the radio–optical properties of the present XRG candidates is underway and will be presented elsewhere (Joshi et al. 2019).

5. Radio Properties of the Present Catalog of XRG Candidates

For the present XRG sample, we have gathered the radio flux density information at several frequencies: at 150 MHz from the TGSS_ADR1 catalog (Intema et al. 2017); at 1.4 GHz from the NRAO VLA Sky Survey (NVSS; Condon et al. 1998); and at 4.85 GHz/5 GHz from the Parkes-MIT-NRAO surveys (PMN, Griffith et al. 1995), the MIT-Green Bank 5 GHz Survey (MIT-GB, Bennett et al. 1986), and the Green Bank 4.85 GHz survey (Becker et al. 1991). These flux densities are listed in Columns (8)–(10) of Tables 2 and 3 for our "strong" and "probable" XRG candidates, respectively. We also list the 1.4 GHz radio luminosity for all the XRG candidates, based on spectroscopic or, alternatively, photometric redshifts. In calculating radio luminosity, we assumed a spectral index $\alpha = -0.8$ (see below). The average luminosity of our strong

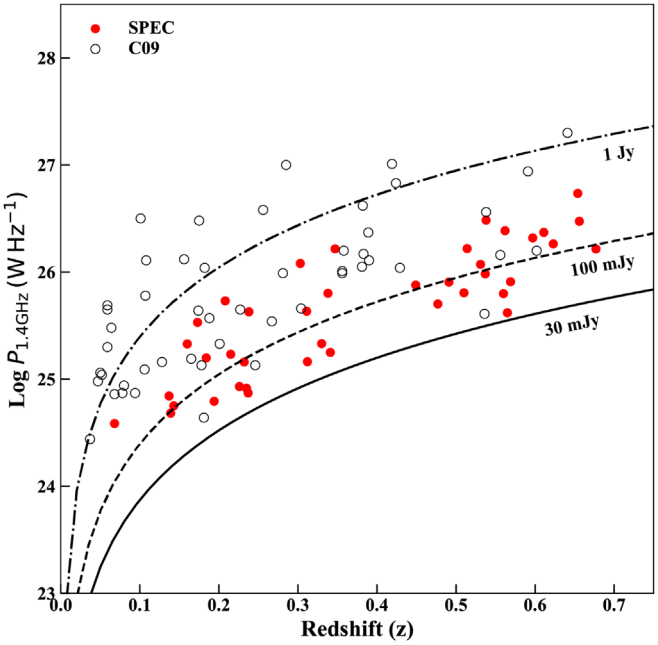

Figure 4. Radio luminosity—redshift diagram for the 40 XRG candidates with available spectroscopic redshift and 1.4 GHz radio luminosity (SPEC). The 50 XRG candidates with available spectroscopic redshifts (Cheung et al. 2009) are shown with black open circles, while our 40 strong XRG candidates are shown with red filled circles. The solid, dashed, and dotted–dashed curves correspond, respectively, to flux densities of 30 mJy, 100 mJy, and 1 Jy, at 1.4 GHz.

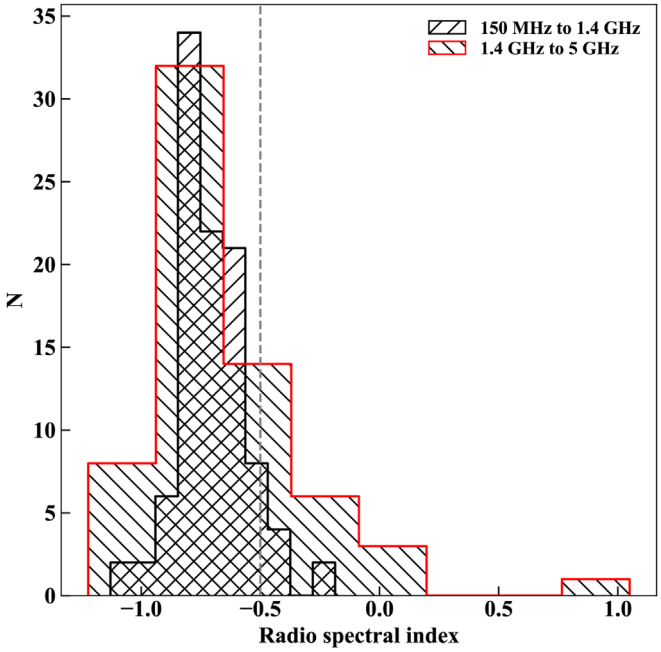

Figure 5. Spectral index distributions for our strong XRG candidates. The red-lined histogram in red color refers to the spectral index (150 MHz–1.4 GHz) values available for 101 strong XRG candidates. The black-lined histogram refers to the spectral index (1.4–5 GHz) values available for 64 of our strong XRG candidates. The vertical dashed line marks the division between the steep (left side) and flat spectra (right side).

XRG candidates with available spectroscopic redshifts is found to be $\log(P_{1.4\,\mathrm{GHz}}) = 25.73$ W Hz^{-1}, with an rms uncertainty of 0.65. This is in agreement with the value given in C07 and is close to the division between the FR I and FR II types (Fanaroff & Riley 1974). Figure 4 displays the 1.4 GHz luminosity versus redshift for our strong XRG candidates with known spectroscopic redshifts. It is seen that our XRG candidates have systematically lower radio luminosity compared to the previously reported XRGs (Cheung et al. 2009). Interestingly, among our "strong" XRG candidates, four objects, namely, J0004+1248, J0028−0026, J0932+1611, and J1324+4334, have a physical size of about 0.80, 0.90, 0.83, and 0.91 Mpc, respectively, in the FIRST 1.4 GHz map (measured as the separation between the ends of the two active radio lobes), and these belong to the family of giant radio galaxies (Willis et al. 1974; Dabhade et al. 2019). Figure 1 shows one of these four giant XRGs, J0004+1248.

For our strong XRG candidates, we have determined the spectral index ($S_i \propto \nu^{\alpha}$) between 150 MHz and 1.4 GHz ($\alpha_{0.15}^{1.4}$) and also between 1.4 and 5 GHz ($\alpha_{1.4}^{5}$), based on the flux densities listed in Table 2. Thus, $\alpha_{0.15}^{1.4}$ could be determined for 101 of our strong XRG candidates, out of which 9 (∼9%) sources are found to have a flat radio spectrum ($\alpha_{0.15}^{1.4} > -0.5$). In addition, $\alpha_{1.4}^{5}$ could be measured for 64 of our strong candidates, with 14 (∼22%) of them showing a flat radio spectrum and 3 out of these 14 actually showing an inverted radio spectrum (i.e., $\alpha_{1.4}^{5} > 0$). The XRG candidates showing a flat/inverted radio spectrum would be particularly valuable for probing the dual-AGN scenario for the origin of X-shaped morphology (e.g., Lal & Rao 2007). Histograms of the two spectral indices for our strong XRG candidates are shown in Figure 5. Both distributions peak near $\alpha = -0.8$.

6. Discussion

6.1. Classification as "Strong" or "Probable" XRG Candidates

The vast majority in the "strong" category are likely to be confirmed as bona fide XRGs, with a pair of radio wings comparable in extent to their active counterparts, the two primary radio lobes. In this section we briefly comment on the justification for including some sources in the present catalog, despite only a marginal evidence for a secondary lobe pair (wings) in their existing radio maps. This stems from the recognition that clear visibility of wings can be hampered owing to a number of factors related to the source evolution/orientation and their directional offset from the primary lobe pair. These difficulties may be compounded by observational limitations related to angular resolution and/or the sensitivity to diffuse emission at the frequency of radio imaging (see, e.g., Wang et al. 2003; Cheung 2007; Cheung et al. 2009). As an example, the XRG candidates J0941+2147, J1206+3812, and J1444+4147 were included in C07's list despite their showing abnormally short wings. However, the wings stood out clearly in subsequent VLA 1.4 GHz images by Roberts et al. (2018). Guided by this, we have included in our XRG catalog several candidates (e.g., J0028−0026 and J0930+2343) whose secondary lobes size is shorter than ∼50% of the primary lobes, provided a hint of inversion symmetry is discernible in their existing radio maps (TGSS_ADR1 and/or FIRST). The classification "strong" has been assigned to some XRG candidates in our catalog, in spite of their radio sizes not being comfortably large enough to reveal their structural details in the existing radio maps. In adopting this somewhat less stringent approach, we have been guided by the experience of several

prominent XRGs that had appeared to be only marginally convincing in their earlier (lower-sensitivity/resolution) radio maps. Prominent such examples include NGC 326 (Fanti et al. 1977), 3C 315 (e.g., Mackay 1969; Lal & Rao 2007), and 3C 63 (Harvanek & Hardcastle 1998).

Further, it needs to be borne in mind that the observed faintness and small sizes of the wings could often be artifacts arising from energy losses suffered by the relativistic plasma radiating in these older/fossil radio components. To overcome this limitation, low-frequency radio imaging with sufficiently high angular resolution and sensitivity is mandatory. With a typical expansion velocity of $\sim 0.1c$ (e.g., Tingay et al. 1998; Arshakian & Longair 2004; Machalski et al. 2010; An & Baan 2012), the active lobes would take $\gtrsim 10^6$ yr to grow to their typically observed dimensions ($\sim$30–60 kpc Mezcua et al. 2011, 2012). This duration is comparable to the expected radiative lifetime of the relativistic plasma in the wings at decimeter or shorter wavelengths, once the energy supply to the wings has been cut off, following the putative spin-flip (Gopal-Krishna et al. 1989; Komissarov & Gubanov 1994; Kaiser & Alexander 1997; Kaiser et al. 1997; Mocz et al. 2011; Singh et al. 2016). The consequent fading could easily push one or both radio wings below the detection threshold, unless imaged at a sufficiently low radio frequency. This situation may not be uncommon, as exemplified by the case of J1257+1228 (see Figure 2). All such sources could be classified as "strong" XRG candidates only because at the low frequency (150 MHz) of the TGSS_ADR1 images their wings are *intrinsically* large enough to be resolved and recognized as such. In contrast, the detection of these wings in the 1.4 GHz FIRST survey was hampered owing both to their shorter radiative lifetimes and to the reduced sensitivity of the FIRST survey to extended radio emission.

6.2. The Fanaroff–Riley Classification for X-shaped Radio Galaxies

Radio luminosities of XRGs have been found to fall near the FR I/FR II division (e.g., Dennett-Thorpe et al. 2002). This trend is further strengthened by the present catalog of XRG candidates (Section 5). In the model of Gopal-Krishna et al. (2003, 2012) this property is linked to the formation mechanism of XRGs itself. Going a step further, Cheung et al. (2009) have shown that the XRGs are located near the FR I/FR II dividing line in the "radio–optical luminosity diagram," also known as the Owen–Ledlow plane (Ledlow & Owen 1996). We now briefly examine this issue in relation to the present sample of XRG candidates. It is well known that the active (primary) radio lobes of XRGs are mostly of the FR II type (Leahy & Parma 1992; Saripalli & Roberts 2018), although some XRGs with FR I primary lobes do exist (Leahy & Williams 1984; Jones & McAdam 1992; Murgia et al. 2001). Figure 6 shows the distribution of our XRG candidates (both "strong" and "probable" types) on the Owen–Ledlow plane. For this we have only used a subset of 101 sources from our sample having spectroscopic redshifts and NVSS 1.4 GHz flux density, and we augmented the sample by including the 50 XRGs with spectroscopic redshifts, taken from the compilation of Cheung et al. (2009). The FR dividing line shown in Figure 6 can be parameterized as $\log P_{1.4\,\mathrm{GHz}} = -0.67 M_R + 10.13$, where $P_{1.4\,\mathrm{GHz}}$ is the radio luminosity at 1.4 GHz and M_R is the r-band absolute magnitude of the host galaxy (Wold et al. 2007). It is evident that our XRG candidates are clustered near the dividing line defined above, in accord with C09. Furthermore, a vast majority of our XRG candidates ($\sim$80%–90%) falls above the dividing line, in the region known to be populated predominantly by FR II sources. This is not unexpected, given that the XRG candidates (both "strong" and "probable") in our catalog are mostly consistent with the FR II morphology. Specifically, we find that only 5 out of the 39 "strong" XRG candidates from our sample with spectroscopic redshifts and NVSS 1.4 GHz flux density fall below the Owen–Ledlow dividing line (i.e., in the preferred domain of FR I sources). An inspection of their FIRST radio maps shows that J0956+0001 in fact has a clear FR II morphology, whereas J0727+3956, J1145+1529, and J1407+2722 are too small for a reliable morphological classification. Only the source J0924+4034 has a morphology (see the bottom left panel of Figure 7) clearly reminiscent of the prototypical FR I XRG NGC 326 (which is marked in Figure 6; see Fanti et al. 1977).

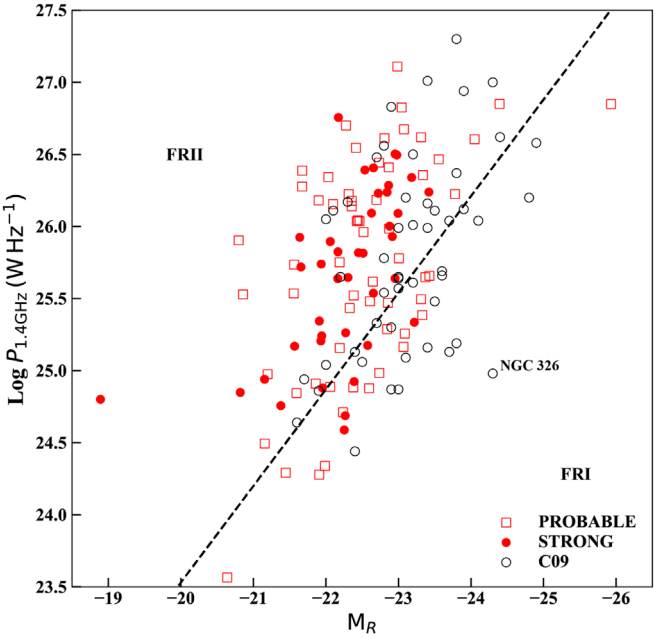

Figure 6. The 1.4 GHz radio luminosity vs. absolute R-band magnitude. The probable and the strong XRG candidates with spectroscopic redshifts are marked with red open squares and red filled circles, respectively. The XRG candidates recompiled in Cheung et al. (2009) are marked with black open circles (C09). The Owen–Ledlow luminosity division line is from Wold et al. (2007). The representative FR I type XRG NGC 326 is marked.

We now turn to the 17 "probable" XRG candidates falling in the FR I region of the Owen–Ledlow diagram, i.e., below the dividing line in Figure 6. Based on the available maps, we found three of them (J0028−0428, J0219+0155, and J1140+1743; see the top row of panels of Figure 7) to show an (inner) morphology reminiscent of the FR I type XRG NGC 326 (see Figure 6 in Murgia et al. 2001). J1140+1743, also known as NGC 3801, has earlier been identified as a Z-shaped source (Hota et al. 2009). We have classified it as a probable XRG (or an intermediate between the X- and Z-shaped radio galaxies) based on its FIRST image shown in the top right panel of Figure 7. As it is known to be a post-merger star-forming galaxy (Hota et al. 2012), its wings could even have formed owing to pre-merger gravitational interaction between the two galaxies. Coming to some other "probable" XRG candidates in the FR I domain (Figure 6), we find that a few of them (e.g., J1044+3540; see the bottom right panel of Figure 7) appear remarkably similar in radio morphology to the early low-resolution radio map of XRG NGC 326 (Fanti et al. 1977), which is a classical example of an FR I XRG, on account of its prominent

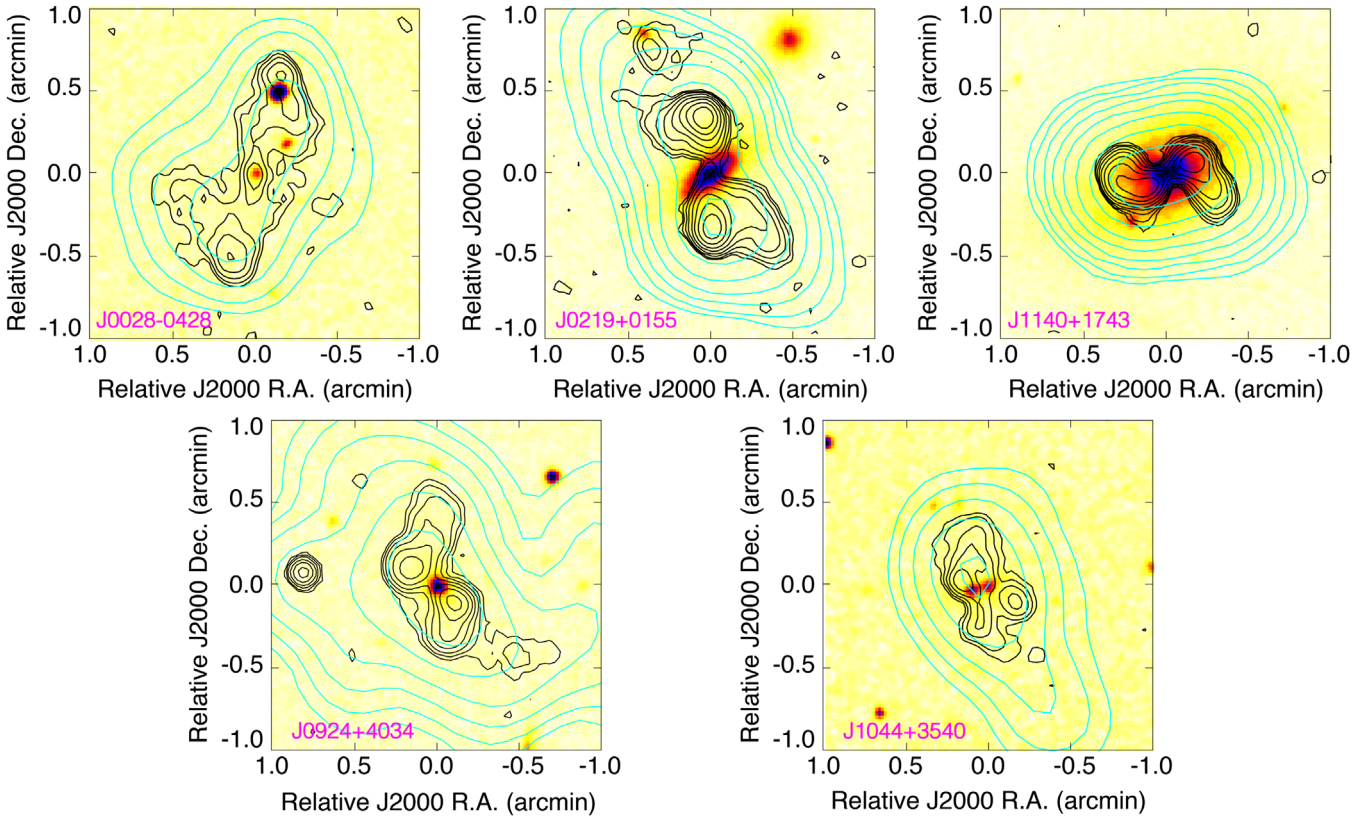

Figure 7. Radio images of the five XRG candidates located in the FR I domain of the Owen–Ledlow diagram. The radio contours are overlaid on the DSS red filter images; the black contours display the FIRST 1.4 GHz maps, and the cyan contours show the TGSS_ADR1 images at 150 MHz. The contours are plotted at (1, 2, 4, 8, 16, 32, ...) × 3σ, where 1σ noise values are 0.19, 0.13, 0.11, 0.16, and 0.15 mJy beam^{-1} for the FIRST maps of J0028−0428, J0219+0155, J1140+1743, J0924+4034, and J1044+3540, respectively, and 3.5 mJy beam^{-1} for all the TGSS_ADR1 maps.

twin jets (Murgia et al. 2001). In relation to such sources, Merritt & Ekers (2002) suggested that if the spin of the active SMBH undergoes a reorientation due to an impulsive torque of external origin, the resulting flip of its spin vector could lead to an X-shaped radio morphology (see also Blandford & Icke 1978; Murgia et al. 2001). On the other hand, a S- or Z-shaped radio morphology would result if the torque operates on the SMBH only gradually, i.e., its duration is longer than the jet outflow timescale. In the case of the radio galaxy NGC 326, an impulsive torque is, in fact, quite plausible, since its host is a dumbbell galaxy composed of a pair of massive ellipticals in gravitational interaction (Battistini et al. 1980). In this scenario, one may expect to find sources with an intermediate morphology (between S/Z-shape and X-shaped), in case the outflow and spin reorientation timescales are comparable.

Speculating on the later evolution of the reoriented (Z/S- and X-shaped) radio sources, Merritt & Ekers (2002) proposed that such sources would eventually evolve into FR II type, on a timescale of $\sim 10^8$ yr. For instance, in the FIRST image of J1009+0529 (Figure 8), the large brightness contrast seen between the active radio lobes and the (much older) wings might be indicative of such a transition in the making, although this remains to be confirmed through spectral index imaging. On the other hand, Saripalli & Subrahmanyan (2009) have proposed an opposite evolutionary scheme (from FR II to FR I), motivated by the examples of FR I radio galaxies in which a newly formed inner lobe pair has been detected, such as 3C 315 and B2014−558. In these sources, whereas the extended primary lobes are of FR I type (Leahy & Williams 1984; Jones & McAdam 1992), their inner doubles show an FR II morphology (de Koff et al. 2000; Saripalli et al. 2008); see also MERLIN 1.6 GHz images of 3C 315 (H. Sanghera & J. P. Leahy, private communication; see http://www.jb.man.ac.uk/atlas/other/3C315.html). However, while the putative evolutionary transition from FR II to FR I morphology may indeed be physically plausible (see also Gopal-Krishna & Wiita 1988), it becomes imperative when the few observed FR I type XRGs are sought to be explained in terms of the backflow deflection model (see Saripalli & Subrahmanyan 2009; Saripalli et al. 2012).

7. Summary and Future Work

Based on a careful visual inspection of the radio sources in the latest release of the VLA FIRST Survey at 1.4 GHz, we have presented here a catalog of 290 winged or XRGs, which almost triples the number of XRG candidates cataloged by Cheung (2007). We classify 106 of them as "strong" (see Figure 9) and 184 as "probable" XRG candidates, which reflects that ∼2%–6% of the radio sources are XRGs. The strong candidates are most likely to be confirmed by follow-up radio observations, while the probable candidates would also be particularly useful for designing future search campaigns for XRGs. The present work extends to smaller angular sizes the XRG search conducted by Cheung (2007), which revealed 100 XRG candidates with a high confirmation rate through follow-up observations. The radio structural information on our XRG candidates has been taken mainly from the FIRST (1.4 GHz), NVSS (1.4 GHz), and TGSS_ADR1 (150 MHz) surveys. Combining this information with the SDSS data, we were able to find optical counterparts for 85 of our 106 strong XRG candidates and 145 of our 184 probable XRG candidates.

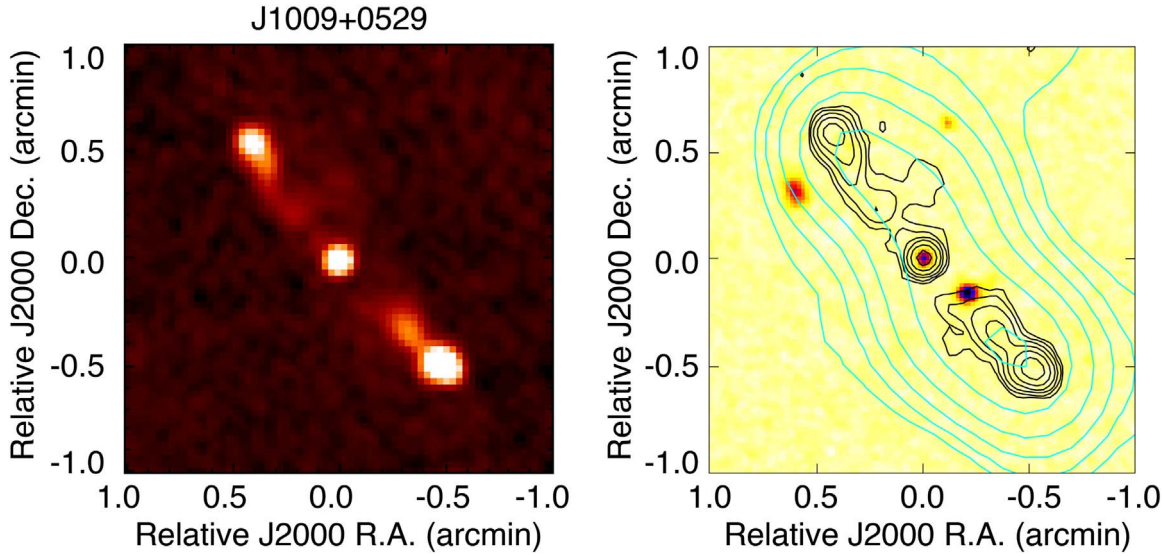

Figure 8. "Probable" XRG candidate J1009+0529 in our catalog; the fields are centered on the optical counterparts. The left panel shows the FIRST gray-scale image, and the right panel shows the FIRST (black) and TGSS_ADR1 (cyan) contours overlaid on the DSS red filter image. Contours levels are set at (1, 2, 4, 8, 16, 32, ...) × 3σ, where 1σ rms noise is 0.18 mJy beam^{-1} for the FIRST map and 3.5 mJy beam^{-1} for the TGSS_ADR1 map.

The corresponding numbers of sources with spectroscopic redshifts are 41 (48%) and 61 (42%), respectively, and the median redshifts are 0.37 and 0.41, respectively. Nine quasars are found among the 106 strong XRG candidates. The sample also contains two strong XRGs showing double-peaked optical emission lines ($z = 0.19$ and 0.33), which makes them excellent candidates for AGNs harboring binary supermassive black holes.

On the radio side, as expected, a vast majority of the present strong XRG candidates are found to have steep radio spectra between 150 MHz and 1.4 GHz, and also between 1.4 GHz and 5 GHz (median $\alpha \sim -0.81$). However, a rather flat radio spectrum ($\alpha > -0.3$) has been found for 10 of our strong XRG candidates. At present, none of them are known to be quasars. Recently, Lal et al. (2019) have shown that in terms of radio spectral index, active lobes do not seem to differ from the (fainter) wings, which may likely support the twin AGN model, where the spectra of the primary lobes and secondary wings are expected to be uncorrelated. It will be interesting to carry out a similar campaign for our bona fide XRGs, in order to place tighter constraints on the models of X-shaped radio sources.

To the extent permitted by the partially complete redshift and radio structural information, we find that the present enlarged sample of XRG candidates adheres to the previously known trend according to which XRGs cluster around the radio luminosity dividing the FR I and FR II radio sources. More specifically, we find that out of our 40 strong XRG candidates with known spectroscopic redshifts and NVSS 1.4 GHz flux, as many as 35 lie above the FR division in the Owen–Ledlow diagram. Even for the five objects falling below the dividing line, an FR II morphology seems quite plausible in most cases. Together with the previously reported samples of XRGs (Cheung 2007; Proctor 2011), the present large sample would allow a closer look into the relative occurrence of X-shaped and Z-shaped radio morphologies among extragalactic radio sources and, in particular, the occurrence of Z-symmetry among the radio wings in XRGs (Gopal-Krishna et al. 2003). In parallel, we are studying the possible relationship of the radio structure to the properties of the host galaxy (Joshi et al. 2019).

This work was supported by the National Key R&D Program of China (2016YFA0400703 and 2018YFA0404603). L.C.H. is supported by the National Key R&D Program of China (2016YFA0400702) and the National Science Foundation of China (11721303). X.F.Y. is supported by the Xinjiang Tianchi Bairen project. R.J. acknowledges support from the China Postdoctoral Science Foundation Grants (2018M630024 and 2019T120011), the National Key R&D Program of China (2016YFA0400702 and 2016YFA0400703) and the National Science Foundation of China (11473002, 11721303, and 11533001). This work makes use of public data from NSF's Karl G. Jansky Very Large Array (VLA); the VLA facility is operated by National Radio Astronomy Observatory (NRAO). The National Radio Astronomy Observatory is a facility of the National Science Foundation operated under cooperative agreement by Associated Universities, Inc. This work uses the public data from the GMRT TGSS survey; we thank the staff of the GMRT that made these observations possible. GMRT is run by the National Centre for Radio Astrophysics of the Tata Institute of Fundamental Research. This work makes use of the Solan Digital Sky Survey data; funding for the Sloan Digital Sky Survey (SDSS) has been provided by the Alfred P. Sloan Foundation, the Participating Institutions, the National Aeronautics and Space Administration, the National Science Foundation, the U.S. Department of Energy, the Japanese Monbukagakusho, and the Max Planck Society. The SDSS website is http://www.sdss.org/. The SDSS is managed by the Astrophysical Research Consortium (ARC) for the Participating Institutions. The Participating Institutions are the University of Chicago, Fermilab, the Institute for Advanced Study, the Japan Participation Group, Johns Hopkins University, Los Alamos National Laboratory, the Max-Planck-Institute for Astronomy (MPIA), the Max-Planck-Institute for Astrophysics (MPA), New Mexico State University, University of Pittsburgh, Princeton University, the United States Naval Observatory, and the University of Washington.

Appendix

Images of 106 "strong" XRG candidates are presented in Figure 9.

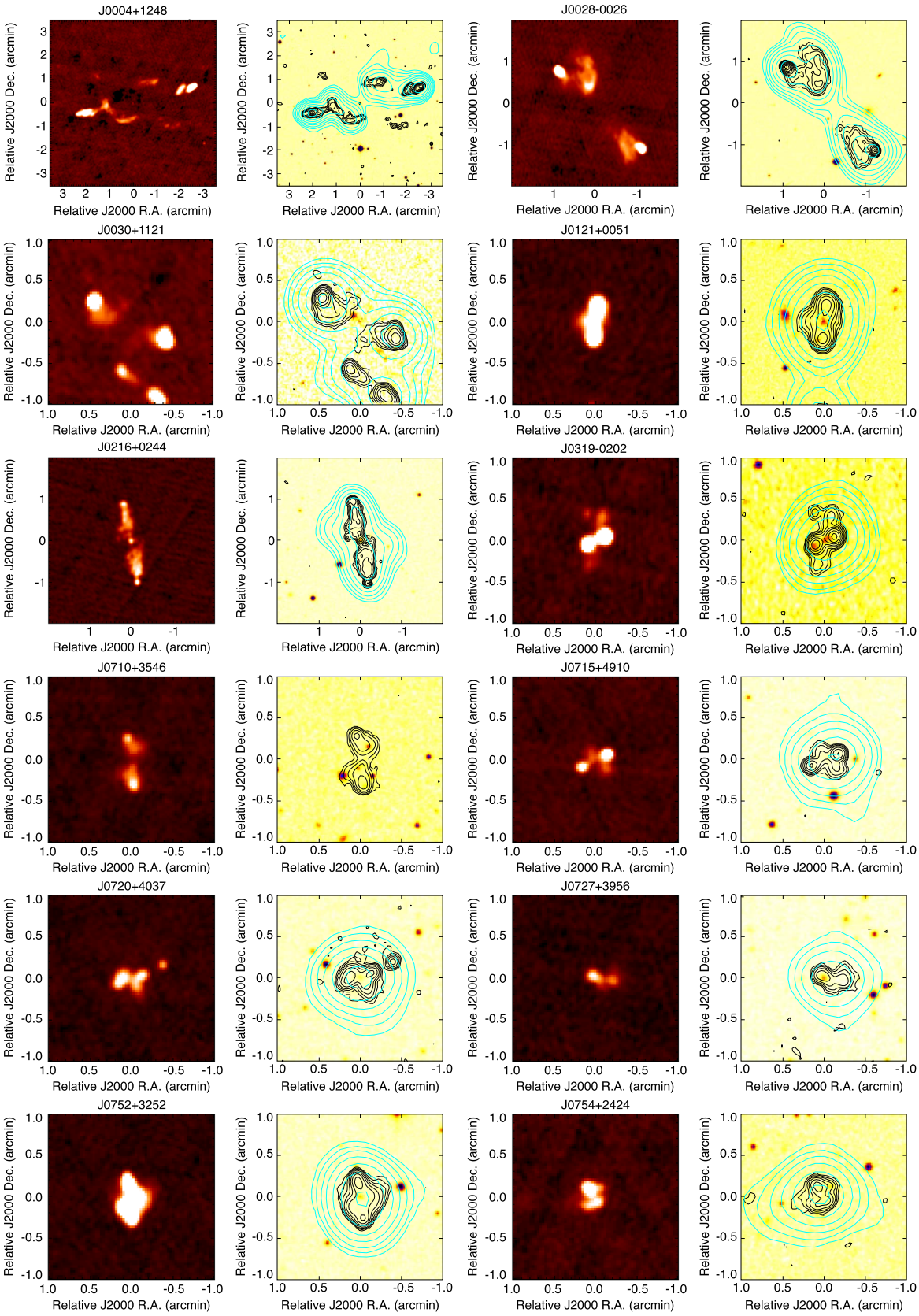

Figure 9. Images of our 106 "strong" X-shaped radio galaxy candidates: VLA FIRST 1.4 GHz images (left figure of each subpanel) and DSS red filter images (right figure of each subpanel) overlaid with TGSS_ADR1 150 MHz (cyan) and VLA FIRST 1.4 GHz contours (black). The fields are centered on the optical counterparts when identified, and otherwise on positions based on the radio morphologies. The radio contours are plotted as $3\sigma \times$ (1, 2, 4, 8, 16, 32, 64, ...), where σ is the rms noise. The rms noise for the 1.4 GHz FIRST images is taken from the VLA FIRST archive. In addition, a median rms noise of 3.5 mJy beam^{-1} is chosen for TGSS_ADR1 fields.

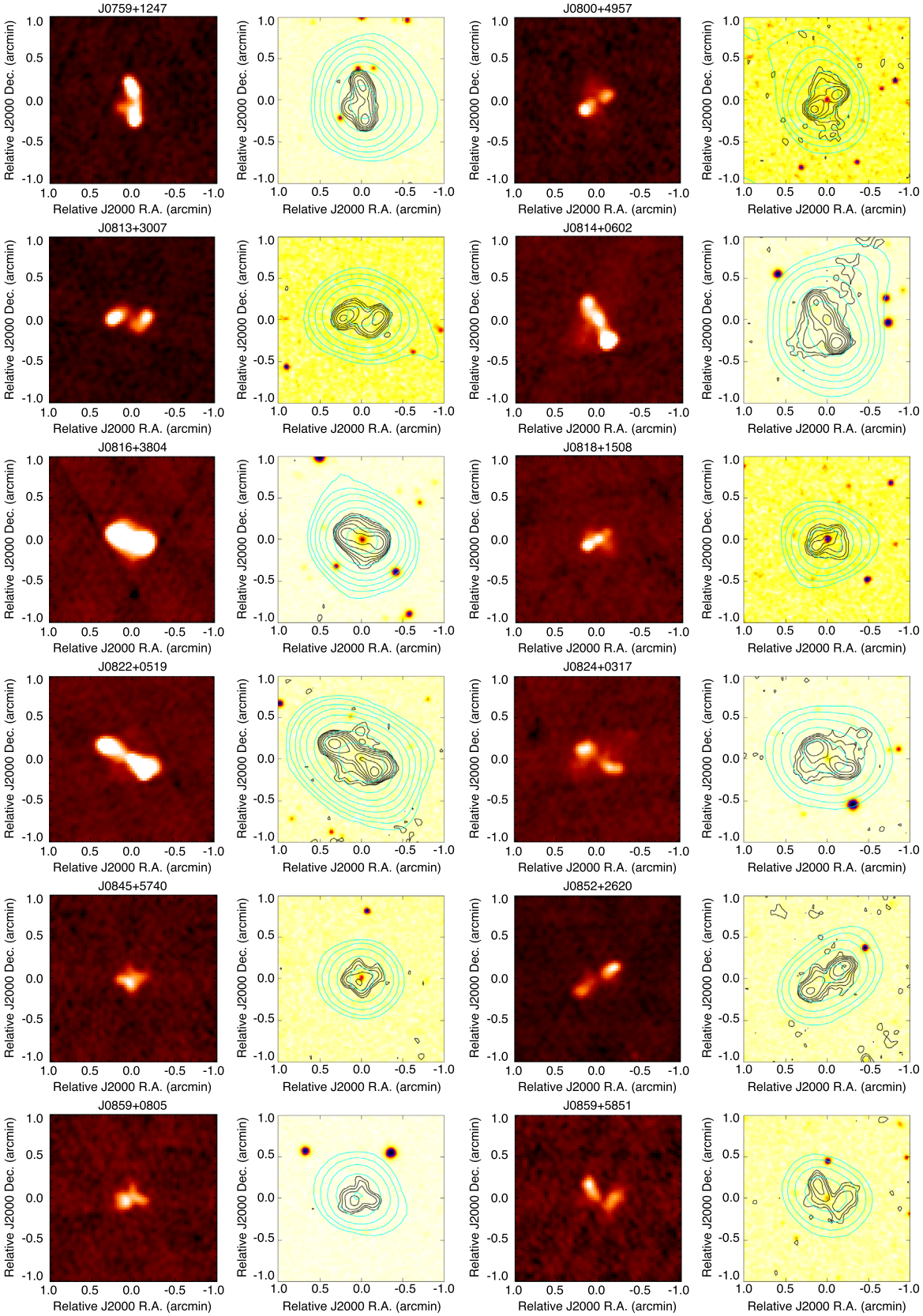

Figure 9. (Continued.)

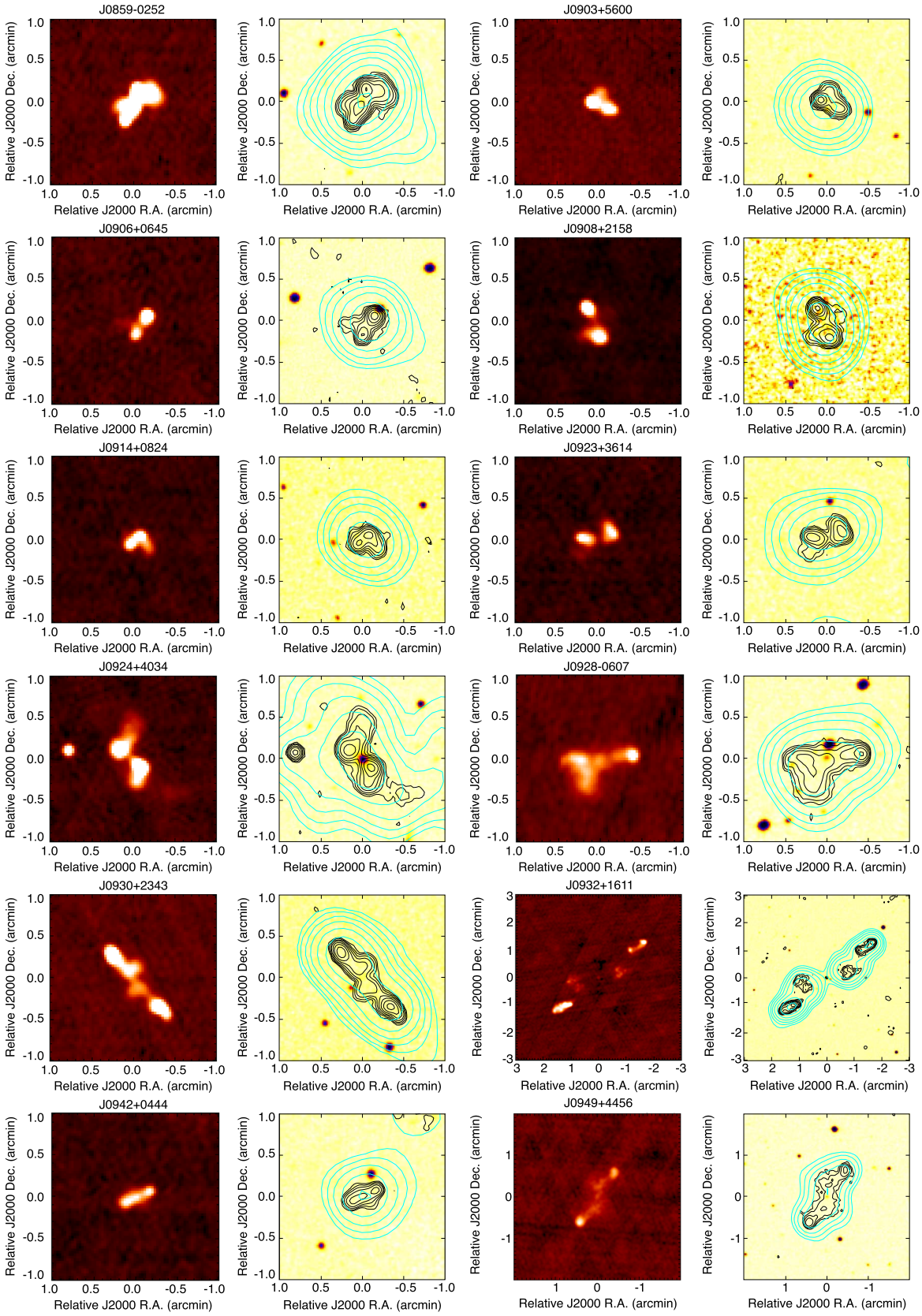

Figure 9. (Continued.)

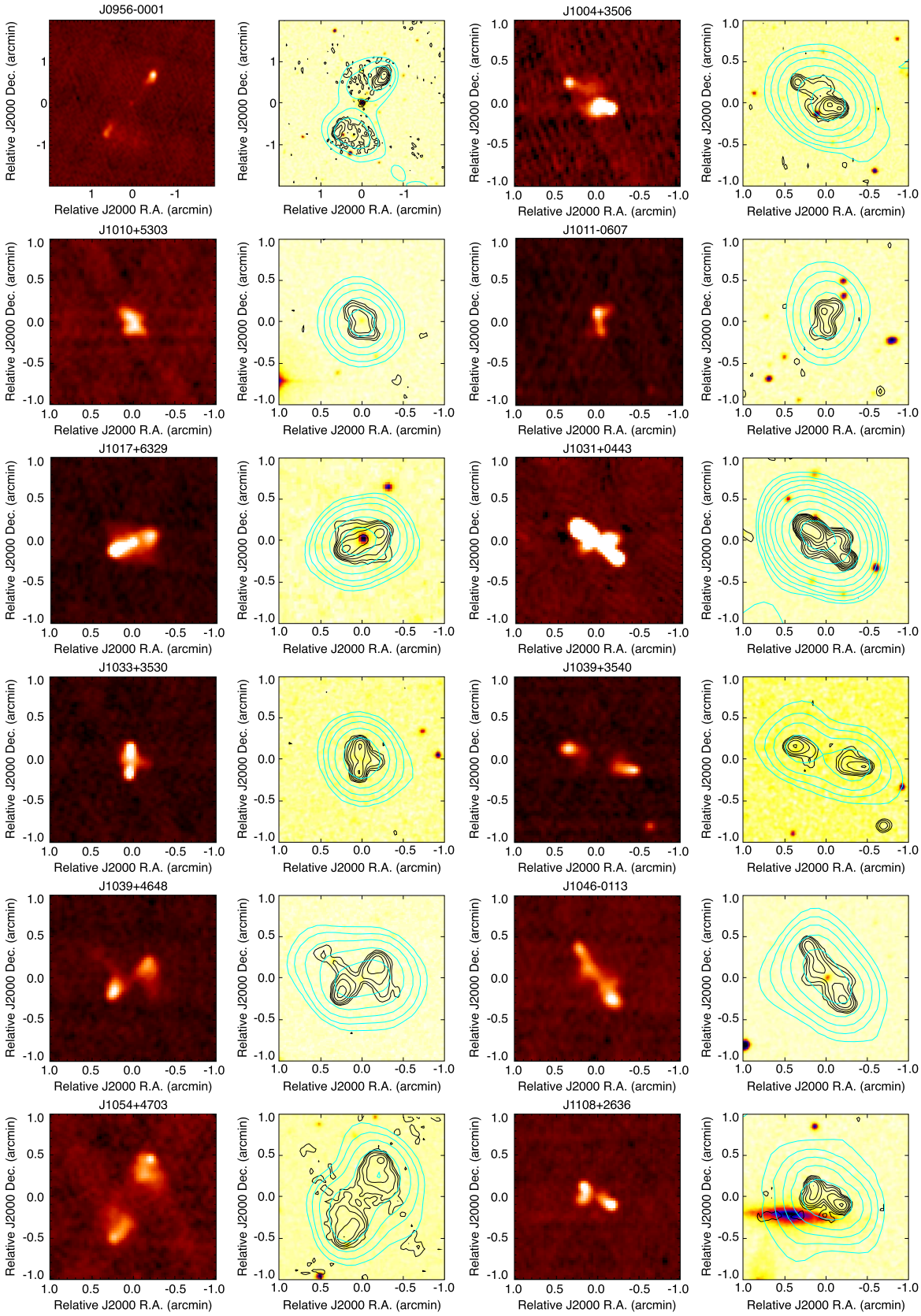

Figure 9. (Continued.)

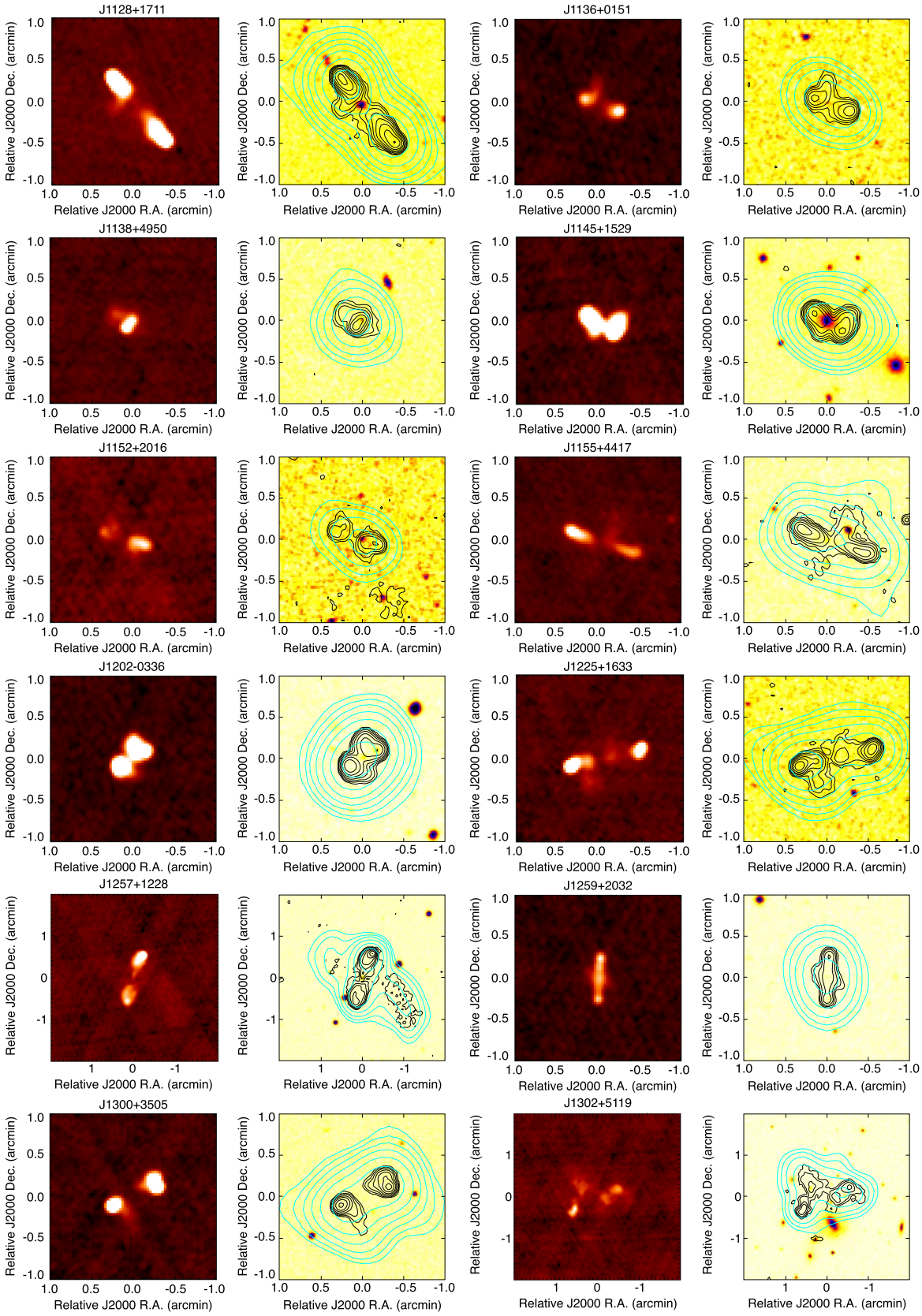

Figure 9. (Continued.)

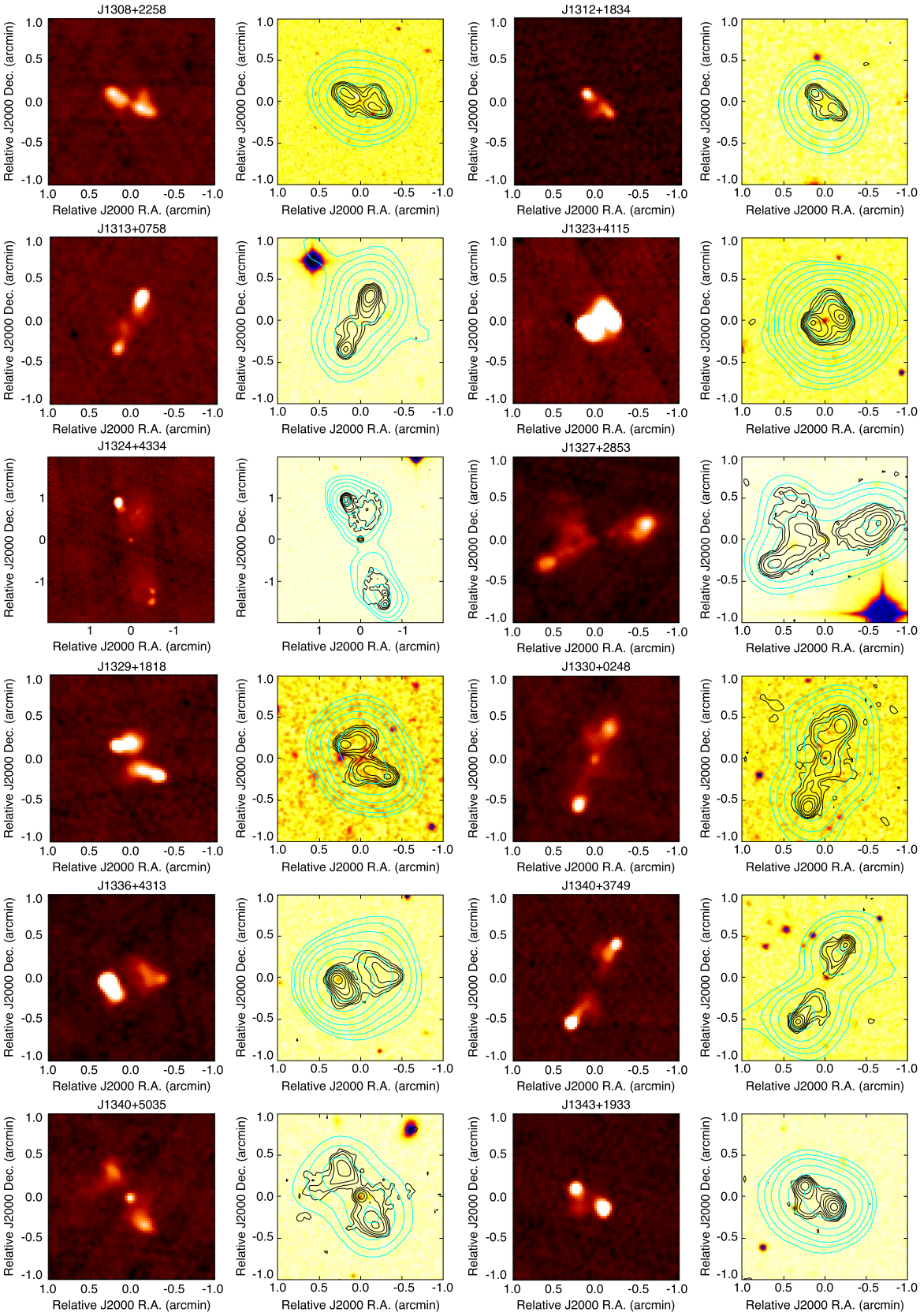

Figure 9. (Continued.)

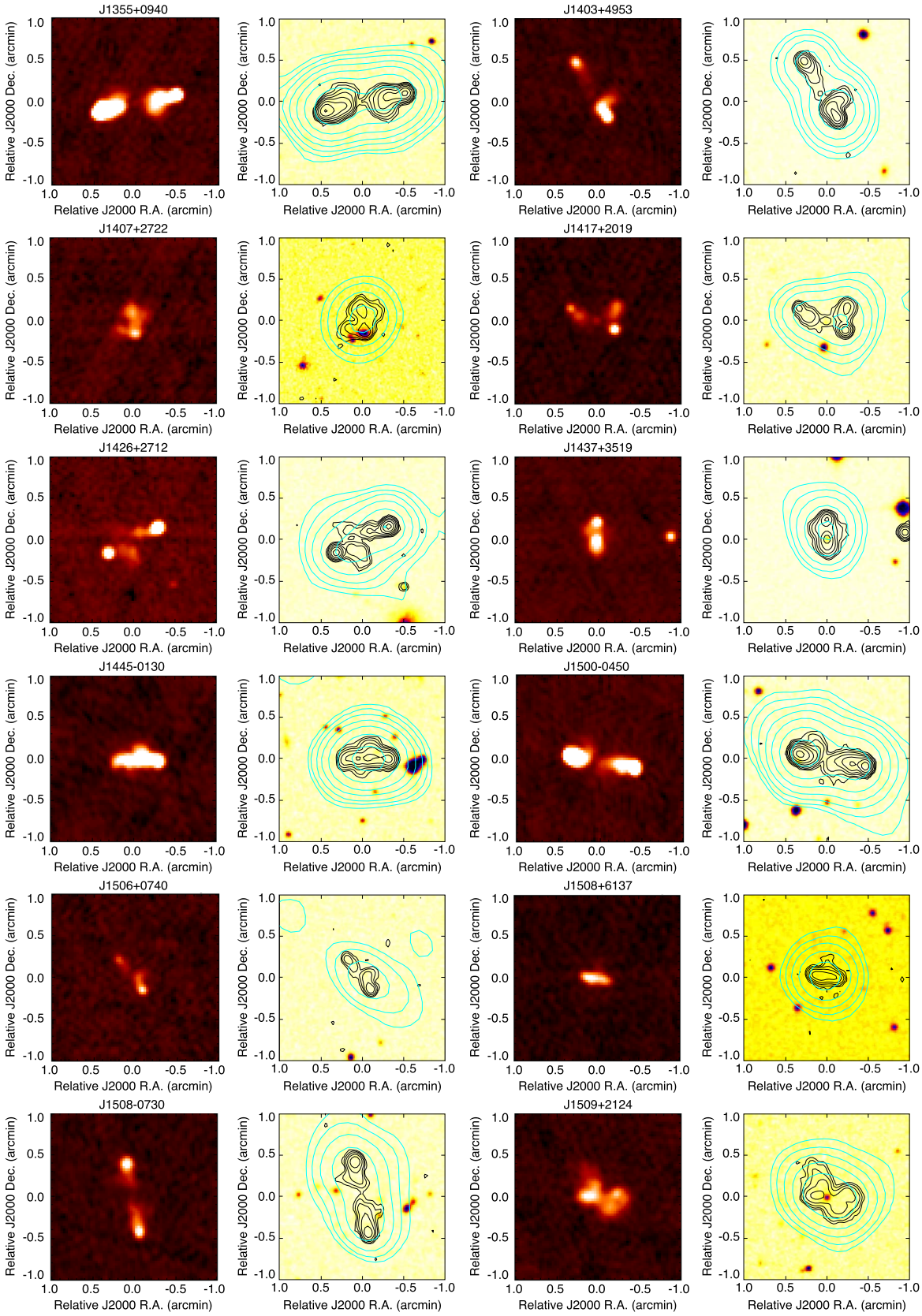

Figure 9. (Continued.)

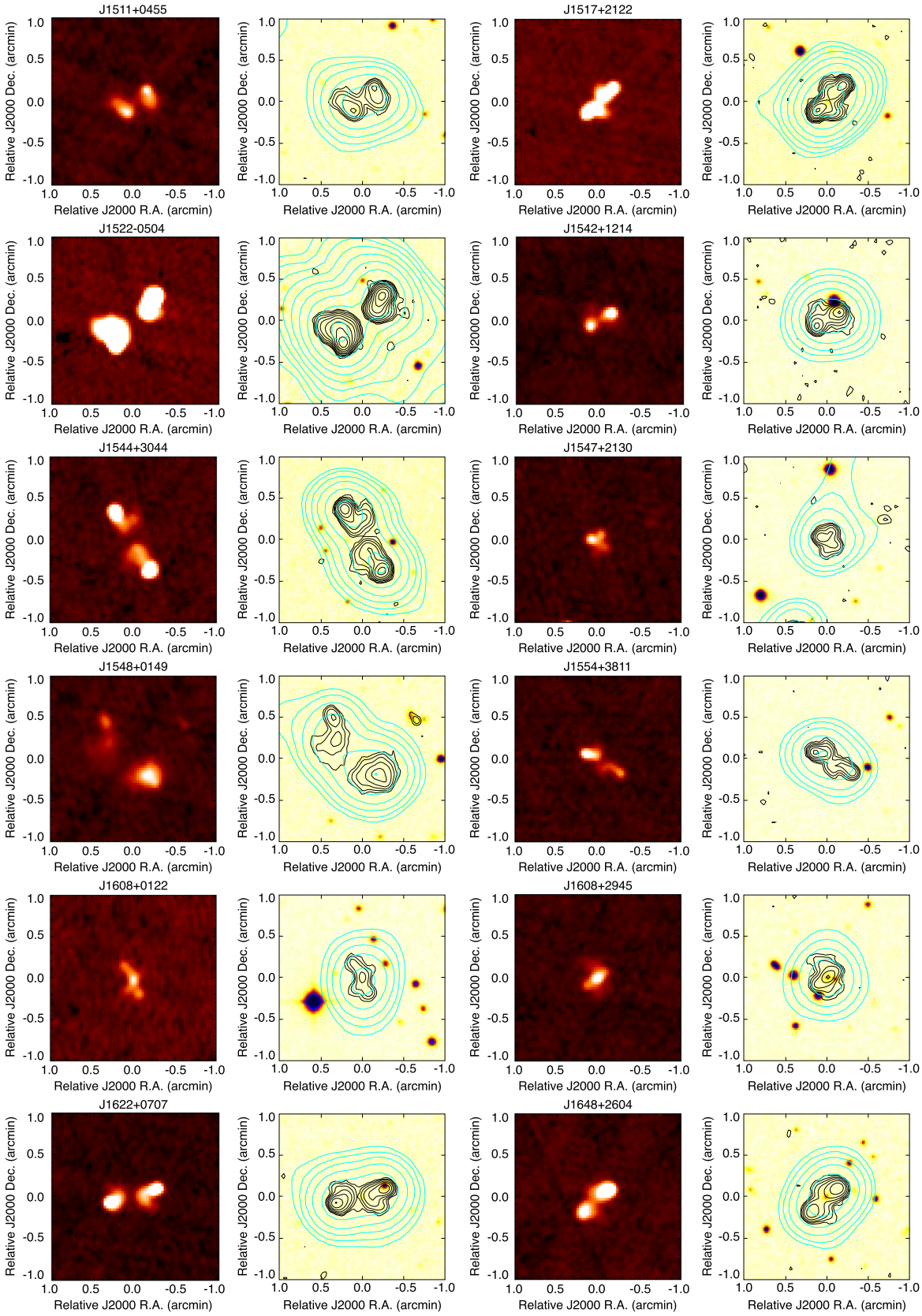

Figure 9. (Continued.)

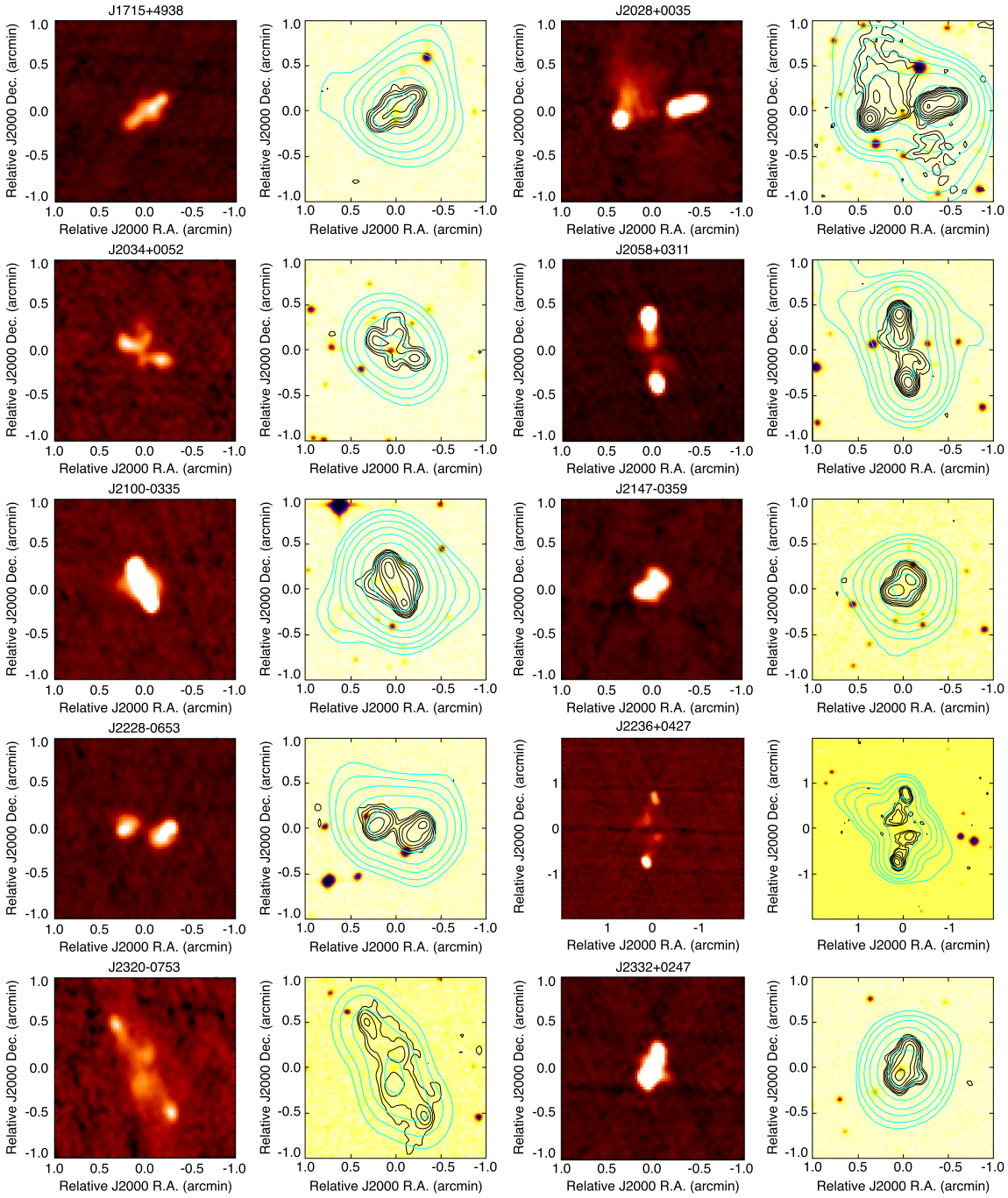

Figure 9. (Continued.)

ORCID iDs

Xiaolong Yang https://orcid.org/0000-0002-4439-5580
Ravi Joshi https://orcid.org/0000-0002-5535-4186
Tao An https://orcid.org/0000-0003-4341-0029
Luis C. Ho https://orcid.org/0000-0001-6947-5846
Ran Wang https://orcid.org/0000-0003-4956-5742

References

An, T., & Baan, W. A. 2012, ApJ, 760, 77
Arshakian, T. G., & Longair, M. S. 2004, MNRAS, 351, 727
Battistini, P., Bonoli, F., Silvestro, S., et al. 1980, A&A, 85, 101
Baum, S. A., Heckman, T. M., Bridle, A., van Breugel, W. J. M., & Miley, G. K. 1988, ApJS, 68, 643
Becker, R. H., White, R. L., & Edwards, A. L. 1991, ApJS, 75, 1
Becker, R. H., White, R. L., & Helfand, D. J. 1995, ApJ, 450, 559
Begelman, M. C., Blandford, R. D., & Rees, M. J. 1980, Natur, 287, 307
Bennett, C. L., Lawrence, C. R., Burke, B. F., Hewitt, J. N., & Mahoney, J. 1986, ApJS, 61, 1
Biermann, P. L., Chirvasa, M., Falcke, H., Markof, S., & Zier, C. 2002, arXiv: astro-ph/0211503
Blandford, R. D., & Icke, V. 1978, MNRAS, 185, 527
Blanton, M. R., & Roweis, S. 2007, AJ, 133, 734
Burke-Spolaor, S. 2011, MNRAS, 410, 2113
Capetti, A., Zamfir, S., Rossi, P., et al. 2002, A&A, 394, 39
Caproni, A., Livio, M., Abraham, Z., & Mosquera Cuesta, H. J. 2006, ApJ, 653, 112

Cheung, C. C. 2007, AJ, 133, 2097
Cheung, C. C., Healey, S. E., Landt, H., Verdoes Kleijn, G., & Jordán, A. 2009, ApJS, 181, 548
Condon, J. J., Cotton, W. D., Greisen, E. W., et al. 1998, AJ, 115, 1693
Dabhade, P., Gaikwad, M., Bagchi, J., et al. 2017, MNRAS, 469, 2886
Dabhade, P., Rottgering, H. J. A., Bagchi, J., et al. 2019, A&A, submitted (arXiv:1904.00409)
de Koff, S., Best, P., Baum, S. A., et al. 2000, ApJS, 129, 33
Dennett-Thorpe, J., Bridle, A. H., Laing, R. A., & Scheuer, P. A. G. 1999, MNRAS, 304, 271
Dennett-Thorpe, J., Scheuer, P. A. G., Laing, R. A., et al. 2002, MNRAS, 330, 609
Ekers, R. D., Fanti, R., Lari, C., & Parma, P. 1978, Natur, 276, 588
Fanaroff, B. L., & Riley, J. M. 1974, MNRAS, 167, 31P
Fanti, C., Fanti, R., Gioia, I. M., et al. 1977, A&AS, 29, 279
Gillone, M., Capetti, A., & Rossi, P. 2016, A&A, 587, A25
Gong, B. P., Li, Y. P., & Zhang, H. C. 2011, ApJL, 734, L32
Gopal-Krishna, Biermann, P. L., Gergely, L. Á, & Wiita, P. J. 2012, RAA, 12, 127
Gopal-Krishna, Biermann, P. L., & Wiita, P. J. 2003, ApJL, 594, L103
Gopal-Krishna, & Chitre, S. M. 1983, Natur, 303, 217
Gopal-Krishna, & Saripalli, L. 1984, A&A, 141, 61
Gopal-Krishna, & Wiita, P. J. 1988, Natur, 333, 49
Gopal-Krishna, Wiita, P. J., & Saripalli, L. 1989, MNRAS, 239, 173
Griffith, M. R., Wright, A. E., Burke, B. F., & Ekers, R. D. 1995, ApJS, 97, 347
Harvanek, M., & Hardcastle, M. J. 1998, ApJS, 119, 25
Heckman, T. M., & Best, P. N. 2014, ARA&A, 52, 589
Heckman, T. M., Smith, E. P., Baum, S. A., et al. 1986, ApJ, 311, 526
Hodges-Kluck, E. J., & Reynolds, C. S. 2011, ApJ, 733, 58
Hodges-Kluck, E. J., Reynolds, C. S., Cheung, C. C., & Miller, M. C. 2010a, ApJ, 710, 1205
Hodges-Kluck, E. J., Reynolds, C. S., Miller, M. C., & Cheung, C. C. 2010b, ApJL, 717, L37
Hogbom, J. A., & Carlsson, I. 1974, A&A, 34, 341
Hota, A., Lim, J., Ohyama, Y., et al. 2009, in ASP Conf. Ser. 401, The Low-Frequency Radio Universe, ed. D. J. Saikia (San Francisco, CA: ASP), 104
Hota, A., Rey, S.-C., Kang, Y., et al. 2012, MNRAS, 422, L38
Intema, H. T., Jagannathan, P., Mooley, K. P., & Frail, D. A. 2017, A&A, 598, A78
Jones, P. A., & McAdam, W. B. 1992, ApJS, 80, 137
Joshi, R., Gopal-Krishna, Yang, X., et al. 2019, arXiv:1911.00016
Kaiser, C. R., & Alexander, P. 1997, MNRAS, 286, 215
Kaiser, C. R., Dennett-Thorpe, J., & Alexander, P. 1997, MNRAS, 292, 723
Komissarov, S. S., & Gubanov, A. G. 1994, A&A, 285, 27
Kormendy, J., & Ho, L. C. 2013, ARA&A, 51, 511
Kraft, R. P., Hardcastle, M. J., Worrall, D. M., & Murray, S. S. 2005, ApJ, 622, 149
Lal, D. V., Hardcastle, M. J., & Kraft, R. P. 2008, MNRAS, 390, 1105
Lal, D. V., & Rao, A. P. 2007, MNRAS, 374, 1085
Lal, D. V., Sebastian, B., Cheung, C. C., & Pramesh Rao, A. 2019, AJ, 157, 195
Landt, H., Cheung, C. C., & Healey, S. E. 2010, MNRAS, 408, 1103
Landt, H., Perlman, E. S., & Padovani, P. 2006, ApJ, 637, 183
Leahy, J. P., Black, A. R. S., Dennett-Thorpe, J., et al. 1997, MNRAS, 291, 20
Leahy, J. P., & Parma, P. 1992, in Proc. 7th I.A.P. Meeting, Extragalactic Radio Sources: From Beams to Jets, ed. J. Roland, H. Sol, & G. Pelletier (Cambridge: Cambridge Univ. Press), 307
Leahy, J. P., & Williams, A. G. 1984, MNRAS, 210, 929
Ledlow, M. J., & Owen, F. N. 1996, AJ, 112, 9
Lotz, J. M., Jonsson, P., Cox, T. J., & Primack, J. R. 2008, MNRAS, 391, 1137
Machalski, J., Jamrozy, M., & Konar, C. 2010, A&A, 510, A84
Machalski, J., Jamrozy, M., Stawarz, Ł., & Weżgowiec, M. 2016, A&A, 595, A46
Mackay, C. D. 1969, MNRAS, 145, 31
Merritt, D., & Ekers, R. D. 2002, Sci, 297, 1310
Mezcua, M., Chavushyan, V. H., Lobanov, A. P., & León-Tavares, J. 2012, A&A, 544, A36
Mezcua, M., Lobanov, A. P., Chavushyan, V. H., & León-Tavares, J. 2011, A&A, 527, A38
Miller, B. P., & Brandt, W. N. 2009, ApJ, 695, 755
Milosavljević, M., & Merritt, D. 2003, in AIP Conf. Proc. 686, The Astrophysics of Gravitational Wave Sources, ed. J. M. Centrella (Melville, NY: AIP), 201
Mocz, P., Fabian, A. C., & Blundell, K. M. 2011, MNRAS, 413, 1107
Murgia, M., Parma, P., de Ruiter, H. R., et al. 2001, A&A, 380, 102
Myers, S. T., & Spangler, S. R. 1985, ApJ, 291, 52
Proctor, D. D. 2003, JEI, 12, 398
Proctor, D. D. 2006, ApJS, 165, 95
Proctor, D. D. 2011, ApJS, 194, 31
Ramos Almeida, C., Tadhunter, C. N., Inskip, K. J., et al. 2011, MNRAS, 410, 1550
Roberts, D. H., Cohen, J. P., Lu, J., Saripalli, L., & Subrahmanyan, R. 2015a, ApJS, 220, 7
Roberts, D. H., Saripalli, L., & Subrahmanyan, R. 2015b, ApJL, 810, L6
Roberts, D. H., Saripalli, L., Wang, K. X., et al. 2018, ApJ, 852, 47
Rossi, P., Bodo, G., Capetti, A., & Massaglia, S. 2017, A&A, 606, A57
Rottmann, H. 2001, PhD thesis, Bonn Univ.
Saripalli, L., & Roberts, D. H. 2018, ApJ, 852, 48
Saripalli, L., & Subrahmanyan, R. 2009, ApJ, 695, 156
Saripalli, L., Subrahmanyan, R., Laskar, T., & Koekemoer, A. 2008, arXiv:0806.3518
Saripalli, L., Subrahmanyan, R., Thorat, K., et al. 2012, ApJS, 199, 27
Singh, V., Ishwara-Chandra, C. H., Kharb, P., Srivastava, S., & Janardhan, P. 2016, ApJ, 826, 132
Tingay, S. J., Jauncey, D. L., Reynolds, J. E., et al. 1998, AJ, 115, 960
Véron-Cetty, M. P., & Véron, P. 2001, A&A, 375, 791
Wang, T.-G., Zhou, H.-Y., & Dong, X.-B. 2003, AJ, 126, 113
White, R. L., Becker, R. H., Helfand, D. J., & Gregg, M. D. 1997, ApJ, 475, 479
Willis, A. G., Strom, R. G., & Wilson, A. S. 1974, Natur, 250, 625
Wirth, A., Smarr, L., & Gallagher, J. S. 1982, AJ, 87, 401
Wold, M., Lacy, M., & Armus, L. 2007, A&A, 470, 531
Worrall, D. M., Birkinshaw, M., & Cameron, R. A. 1995, ApJ, 449, 93
Zhang, X.-G., Dultzin-Hacyan, D., & Wang, T.-G. 2007, MNRAS, 377, 1215
Zier, C. 2005, MNRAS, 364, 583
Zier, C., & Biermann, P. L. 2001, A&A, 377, 23